

CB 3589

N-Factor Computations for the X-33 Vehicle

P.Balakumar

May 24th 2001

•!

Old Dominion University Research Foundation

N-Factor Computations for the X-33 Vehicle

P.Balakumar

May 24th 2001

!

N-Factor Computations for the X-33 Vehicle

P.Balakumar

May 24th 2001

Abstract

N-Factor computations for the X-33 vehicle on the lower side of the body were performed. The transition prediction code e^{Malik} was used to compute the N-Factors and the meanflow field was computed using the CFL code LAURA. The computations are done at two angles of attack 30 and 40 degrees and the freestream Mach number and Reynolds number are $M= 6$ and $Re = 7.7*10^6$. The N-Factors obtained are very low in the range of 2-3 near the experimentally observed transition onset regions. The stability computations show that at 30 degrees angle of attack, the transition occurs due to crossflow instability and at higher angles of attack the transition occurs due to first mode inviscid instability.

Introduction

In this work, the stability and the transition front on the lower surface of the X-33 vehicle were investigated using the linear stability and the N-Factor method. The mean flow field is computed using the CFD code LAURA (1967) and the N-Factors are computed using the e^{Malik} (Malik 1998) transition prediction code. The computations are performed for $M=6$, $Re = 7.7*10^6$ at two angles of attack 30 and 40 degrees.

Results

The computations are performed for two wind tunnel conditions.

$$\text{Freestream density } \rho_{\infty} = 0.1121 \text{ kg/m}^3$$

$$\text{Freestream velocity } U_{\infty} = 958.28 \text{ m/s}$$

$$\text{Freestream temperature } T_{\infty} = 62.885 \text{ }^{\circ}\text{K}$$

$$\text{Wall temperature } T_w = 366 \text{ }^{\circ}\text{K}$$

$$\text{Angle of attack : Case 1: } 30^{\circ}$$

$$\text{Case 2: } 40^{\circ}$$

Figures 1a, b show the grid distributions used in the CFD menflow computations on the lower surface of the body. The grid size is I=253 and J=61 in the X and Y directions. In the figure 1b, the every 5th grid lines are shown and the grid numbers (I, J) are marked for future reference. The length of the body is 10 inches.

Case 1.

For this case the angle of attack is 30° . Figure 2 shows the streamline pattern at the edge of the boundary layer in the (X, Y) plane. It is seen that there exists an attachment line close to the outer edge. Experimentally, the transition front is observed between this attachment line and the symmetry plane $Y=0$. The stability and the transition computations are performed in this region. Figure 3 shows the Mach contours at the edge of the boundary layer in the (X, Y) plane. It is seen that the Mach numbers at the edge of the boundary layers are in the range of 1 to 2 and along the center line the Mach number is about 1.75. Figure 4 shows the pressure contours on the surface. The computations show that the pressure decreases in the front part and remains constant for most of the part along the centerline. Figure 5 shows the boundary layer profiles along the inviscid streamlines at the $I=20$ and $J = 5, 15, 25, 35, 45$ and 60 stations. Similarly, figures 6-9 show the profiles at different streamwise locations $I = 30, 50, 70, 90$. At $I=20$, the boundary layer thickness is almost constant around 0.05mm and at $I=90$ the boundary layer thickness increases to about 1mm near the symmetry plane $J=60$. It is also observed that the boundary layer thickness increases from 0.2mm near the outward stations $J=5$ to 1mm near the symmetry plane $J=60$.

Figures 10-14 show the crossflow velocity distribution at different I and J stations. As expected, the maximum crossflow velocity occurs in the middle region between the symmetry plane and the attachment line. The maximum crossflow velocity is about 40m/s at $I = 70, 90$ and $J=45$ locations. This is about 5 to 6% of the boundary layer edge velocity. Figures 15-19 show the density distributions and figures 20-24 show the temperature distributions. As it is seen the wall temperature is slightly larger than the boundary layer edge temperature. Since cooling the wall stabilizes the instability waves, first mode and the crossflow instability, at low supersonic Mach numbers, the expected N-Factors will be small.

Figures 25-30 show the boundary layer velocity profiles along the inviscid streamline, crossflow velocity profiles and the temperature profiles at stations $I=75$ and $J= 30, 33, 35, 40, 45, 50$. Figure 31 shows the stability results for the most amplified disturbances at these stations. The most amplified waveangles are about 80° and the most amplified frequencies are about 20-25 kHz, implying that the instability is dominated by the crossflow. The largest amplification occurs in the region $J=33-40$, that is in the middle region between the attachment line and the symmetry line where the maximum crossflow occurs. Figure 32 shows the N-Factor traces computed using the e^{Malik} transition prediction code. The computations show that the maximum N-Factors obtained are about 1.7 and it occurs about $X = 18$ cm (7in.), $Y = 3.5$ cm (1.4 in.).

Case 2.

Similarly, figures 33-68 show the results for the Case 2 where the angle of attack is increased to 40°. Figure 33 shows the streamlines pattern, figure 34 shows the Mach contours and figure 35 shows the pressure contours. It is seen that at high angle of attack, the attachment line moves inside towards the center line and the edge Mach numbers are smaller about 1.4 along the centerline. Figures 36-41 show the boundary layer velocity profiles along the inviscid streamline, figures 42-47 show the crossflow velocity profiles. Figures 48-53 show the temperature profiles. It is seen that the boundary layer thickness is about .05mm at the station I=20 and it is about 1mm at I=90 J=60. Another important observation is that the boundary layer profiles after the station I=70 are inflectional. It is also noted that the maximum crossflow velocity is small about 20m/s compared to 40m/s in the earlier lower angle of attack case. The temperature profiles are about constant across the boundary layer.

Figures 54-60 show the streamwise and crossflow velocity profiles and temperature distributions at the station I=75 and at different J=60, 57, 55, 53, 50, 46, 44 stations. Figure 61 shows the stability results at these stations. It is seen that the amplification rates are about two times higher than that for the Case 1. The most amplified waveangles are about 60° and they are located close to the symmetry line. Figures 62 to 66 show the boundary layer profiles at stations I=95 and J=60, 57, 55, 53, 51 and figure 67 shows the linear stability results. The amplification is smaller than that is at I=75, but the most amplified waveangles are about 57° and they are located close to the symmetry line. This shows that the instability is due to the first mode not due to the crossflow and it is expected that transition will first occur along the symmetry line. The strong instability in this case along the centerline is due to the inflectional profiles. Figure 68 shows the N-Factor traces obtained from the e^{Malik} transition prediction code and as it is expected the N-Factors are larger near the symmetry line. However, the maximum N-Factors are small in the range of 3 at X= 18cm (7in.).

Discussion and Conclusions

Stability and N-Factor computations are performed for the boundary layer profiles at the lower surface of the X-33 vehicle. The computations are done for two cases, one at a lower angle of attack of 30 degrees and the other at a higher angle of attack 40 degrees. At 30 degrees angle of attack, the transition is dominated by the crossflow instability and the flow is most unstable in the middle region between the symmetry line and the

attachment line, which exists closer to the outer edge. At 40 degrees angle of attack, the crossflow velocity becomes small and the boundary layer profiles become inflectional closer to the centerline. This makes the flow to be very unstable near the symmetry line and the instability is due to firstmode inviscid type instability. However, the N-factors obtained are very small in the order of 1.75 in the first case and about 3 in the second case. This due to the fact that wall temperature is very low 366 °K and the edge temperature is about 300 °K and this makes the first mode and the crossflow instabilities to be very stable. In figures 69-71, the experimental results are presented. Figures 69 and 70 show the wall temperature measurements along the symmetry line for the two cases. It is seen that transition occurs around 6 in. for the 30 degrees case and it occurs around 5 in. for the 40 degrees case. Figure 71 shows the experimentally observed transition front for the 30 and 40 degrees cases. It is seen that at lower angle of attack , the transition front appears as two parabolas located symmetrically about the centerline and at 40 degrees both parabolas merge and becomes a single parabola and the transition first occurs along the centerline. These observations agree with the calculations, but the N-Factors at the transition onset points are very small. There may be several reasons, one may be that the freestream disturbances may be large and this causes early transition.

References

- Cheatwood, F. M. and Gnoffo, P. A., " Users Manual for the Langley Aerothermodynamic Upwind Relaxation Algorithm (LAURA)," NASA TM-4674, April 1996.
- Malik, M. R., "eMalik3d: An e^N Code for Three-Dimensional Flow over Finite-Swept Wings," HTC Report No. HTC-9502 (Version 2), 1995.
- Thompson, R. A., Hamilton, H. H. , Berry, S. A., Horvath, T. J. and Nowak, R. J., " Hypersonic Boundary-Layer Transition for X-33 Phase II Vehicle," AIAA Paper 98-0867, 1998.

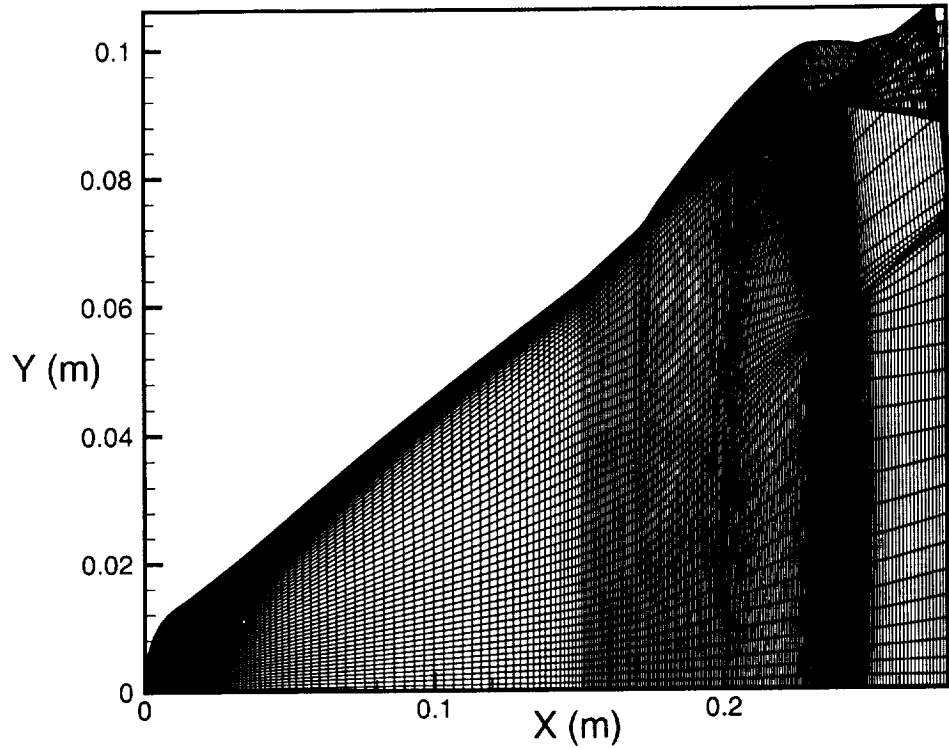


Figure 1a. Grid for X-33 lower surface.

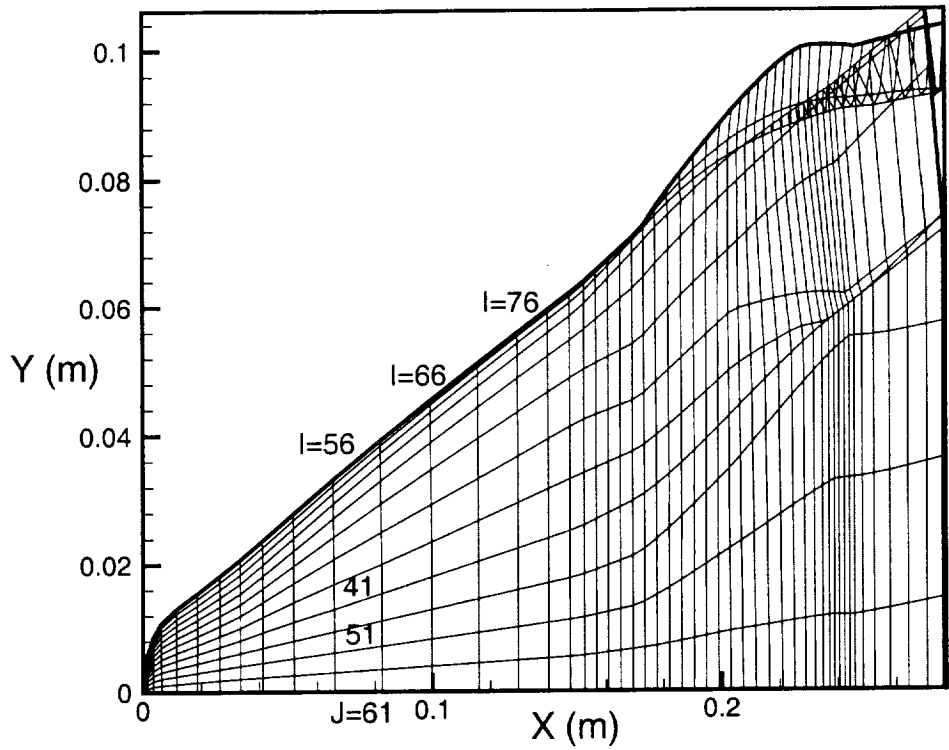


Figure 1b. Grid for X-33 lower surface. Every 5th grid line is shown

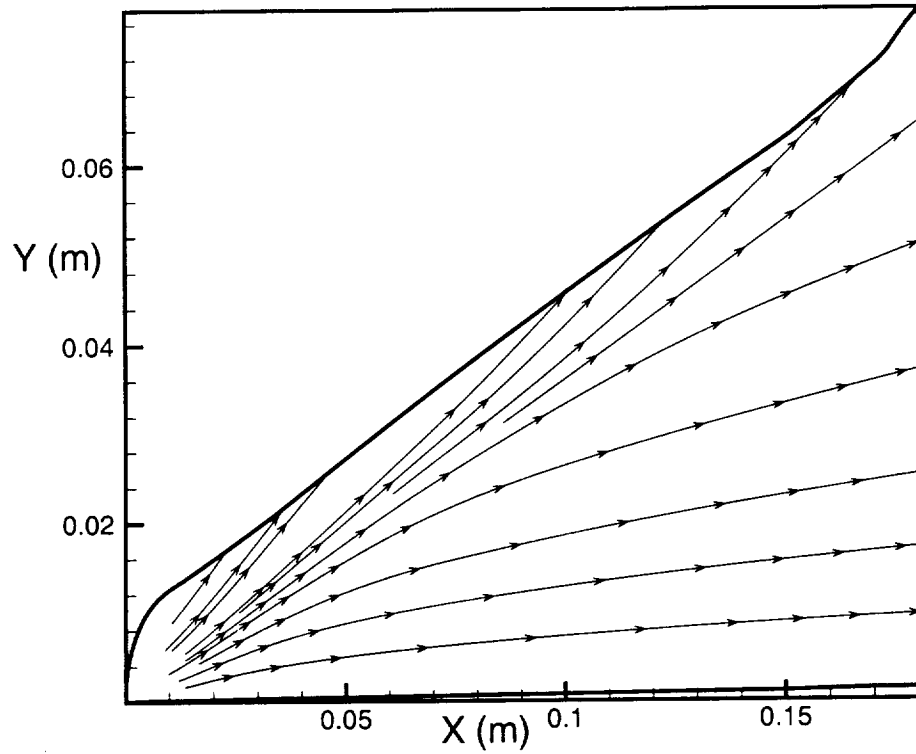


Figure 2. Streamlines pattern.

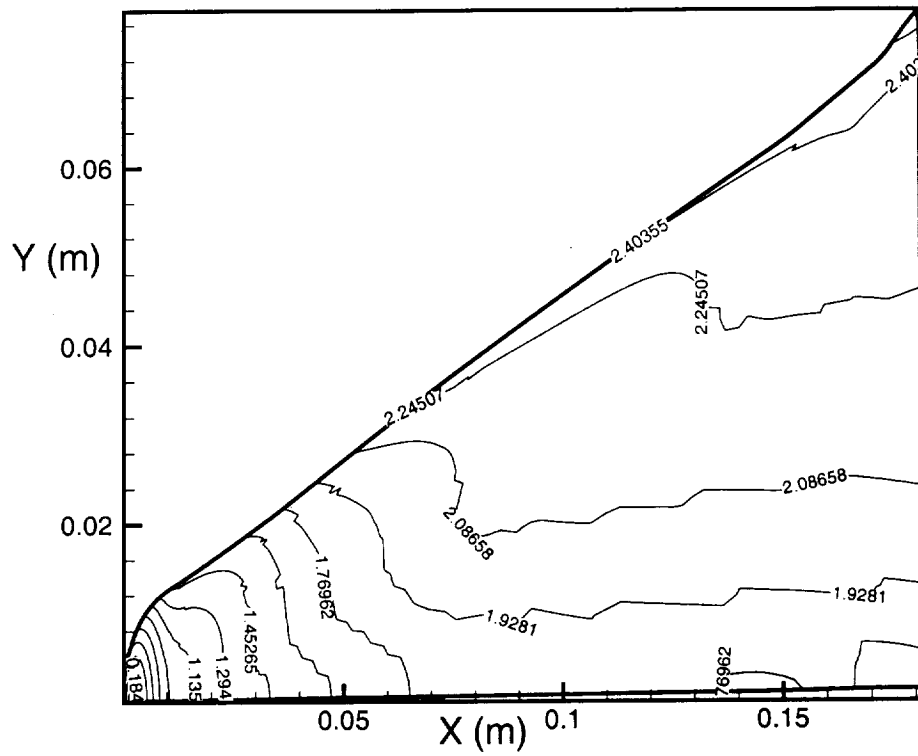


Figure 3. Mach contours.

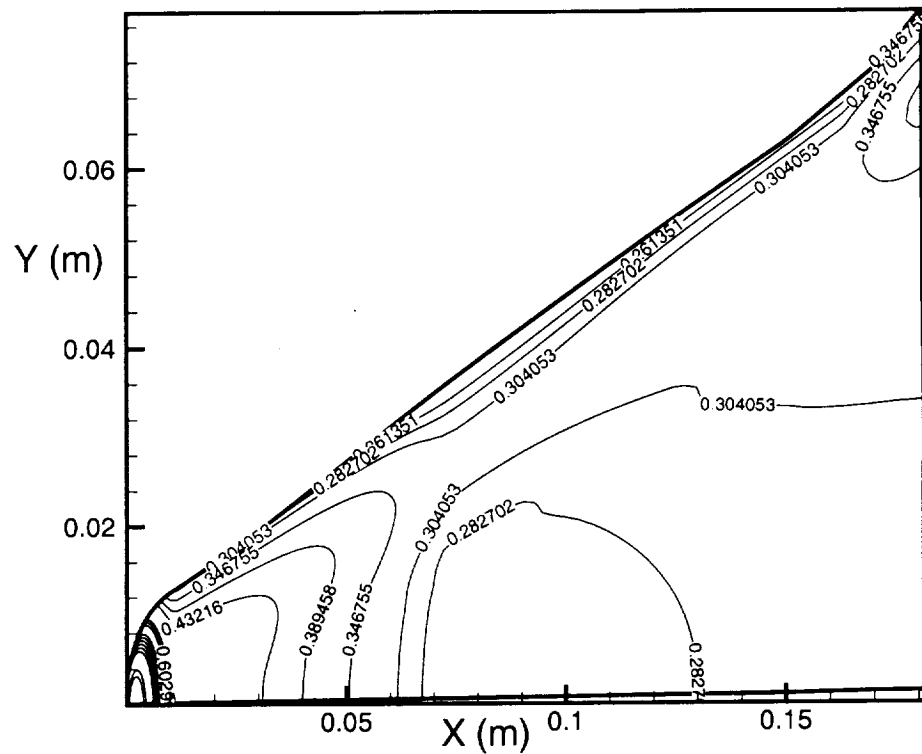


Figure 4. Pressure contours.

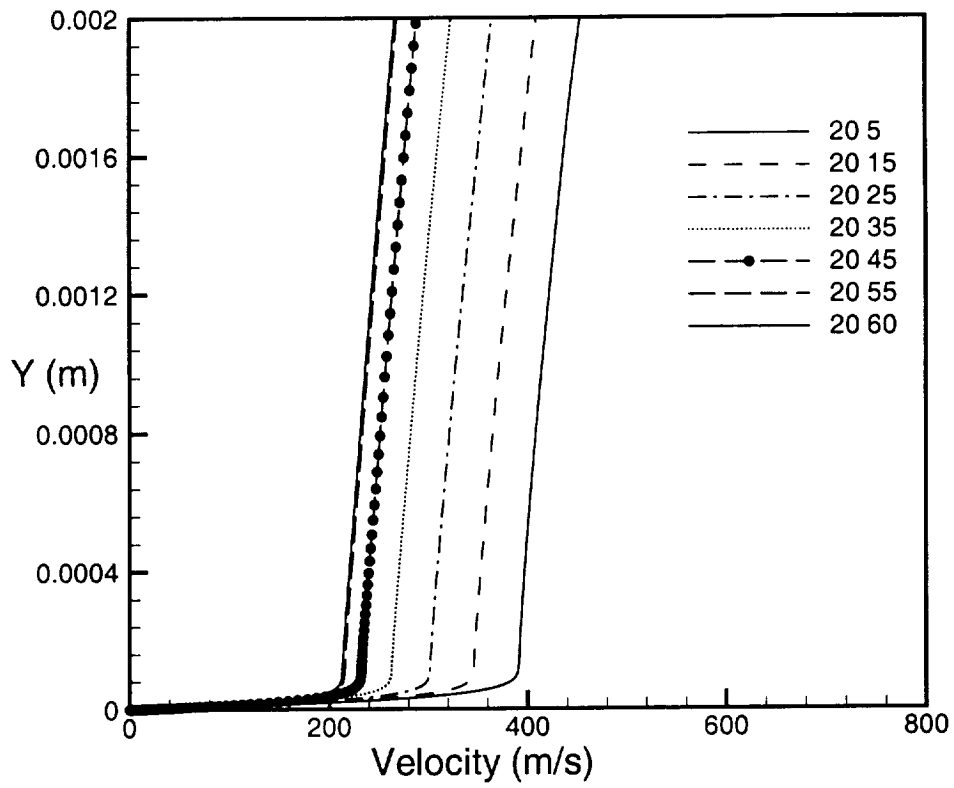


Figure 5. Boundary layer velocity profiles along the inviscid streamlines $I=20$.

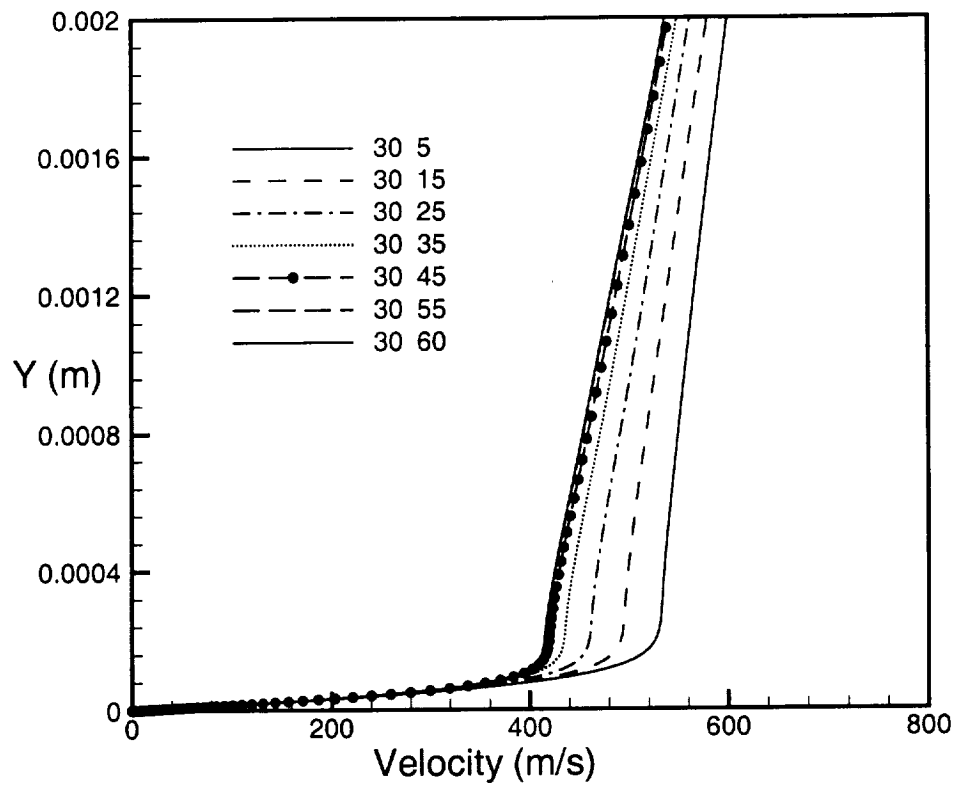


Figure 6. Boundary layer velocity profiles along the inviscid streamlines $I=30$.

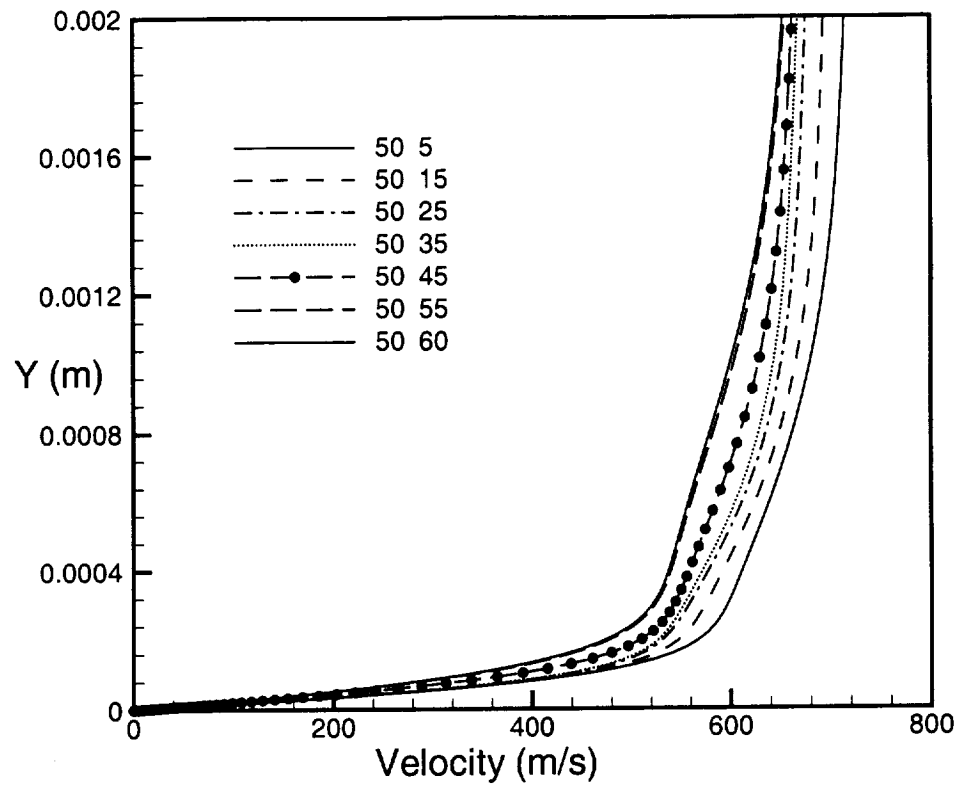


Figure 7. Boundary layer velocity profiles along the inviscid streamlines I=50.

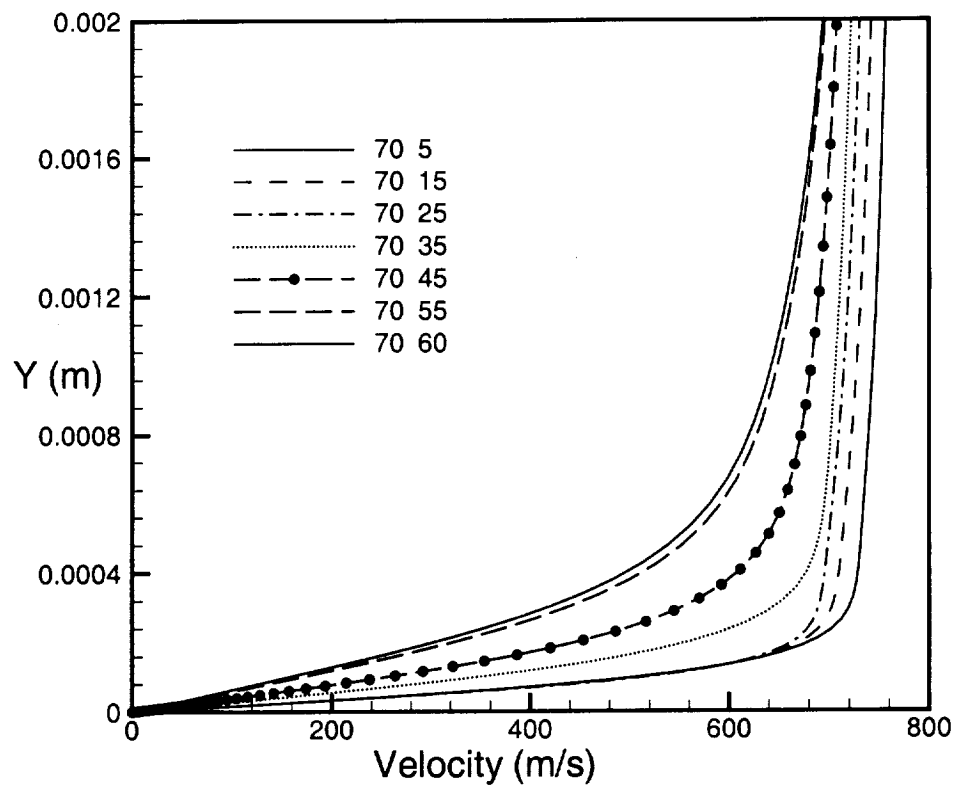


Figure 8. Boundary layer velocity profiles along the inviscid streamlines $I=70$.

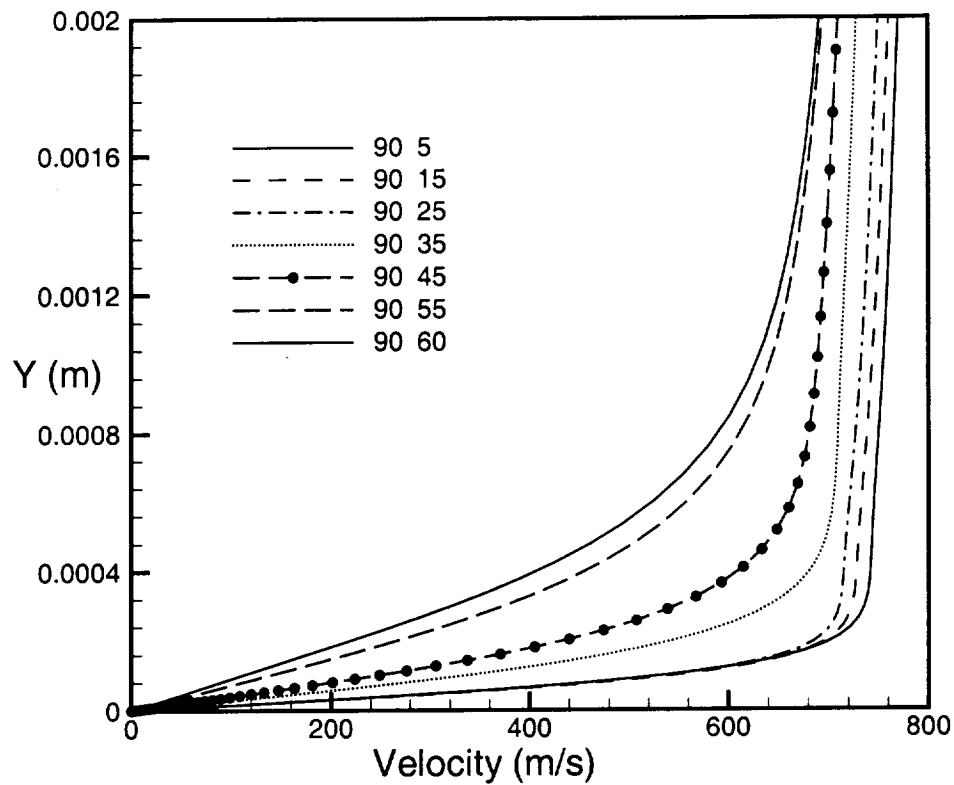


Figure 9. Boundary layer velocity profiles along the inviscid streamlines I=90.

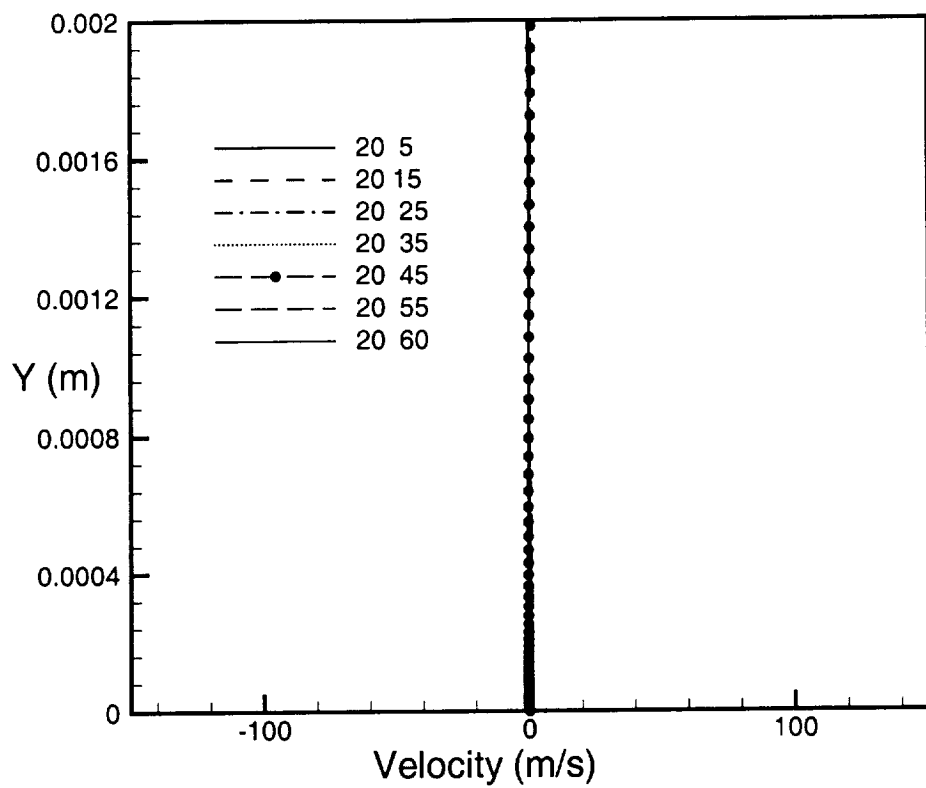


Figure 10. Boundary layer crossflow velocity profiles I=20.

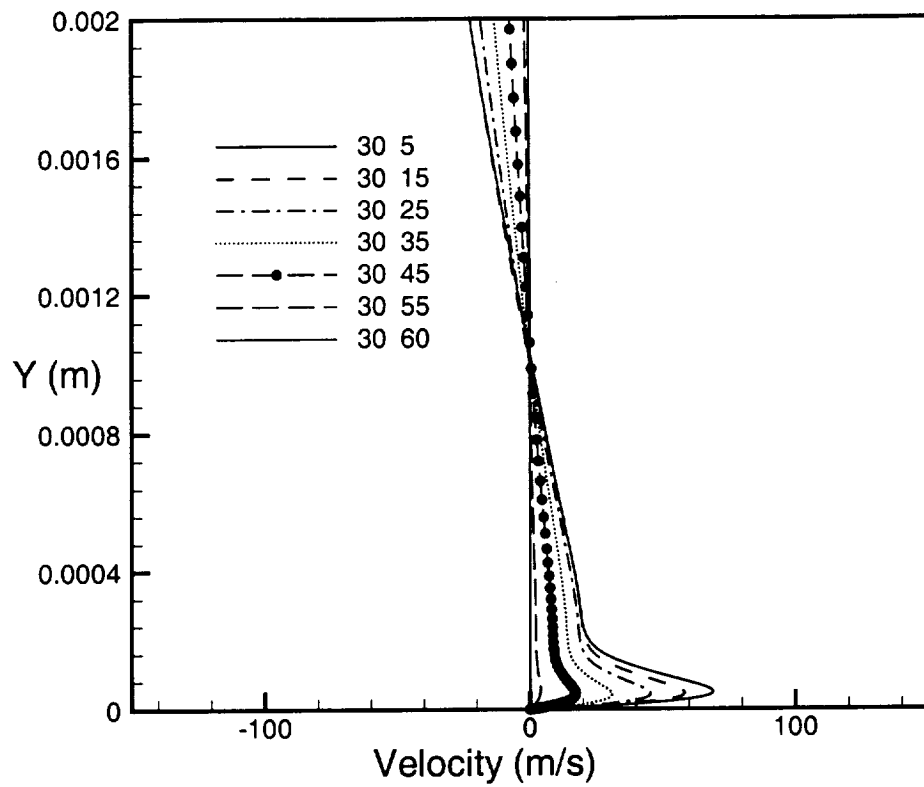


Figure 11. Boundary layer crossflow velocity profiles I=30.

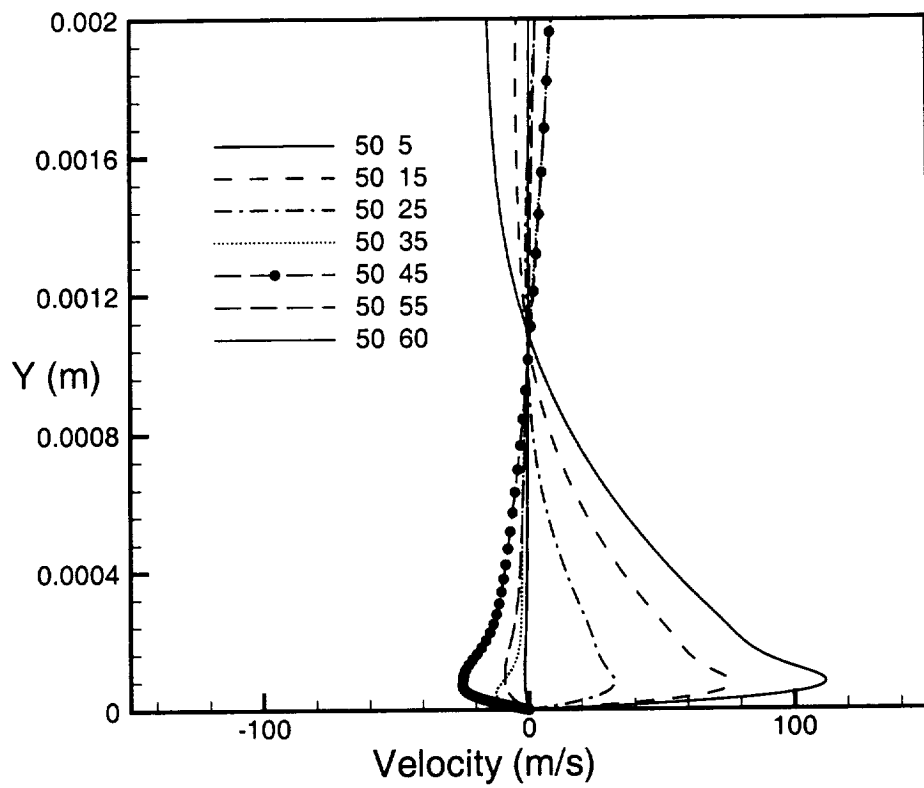


Figure 12. Boundary layer crossflow velocity profiles I=50.

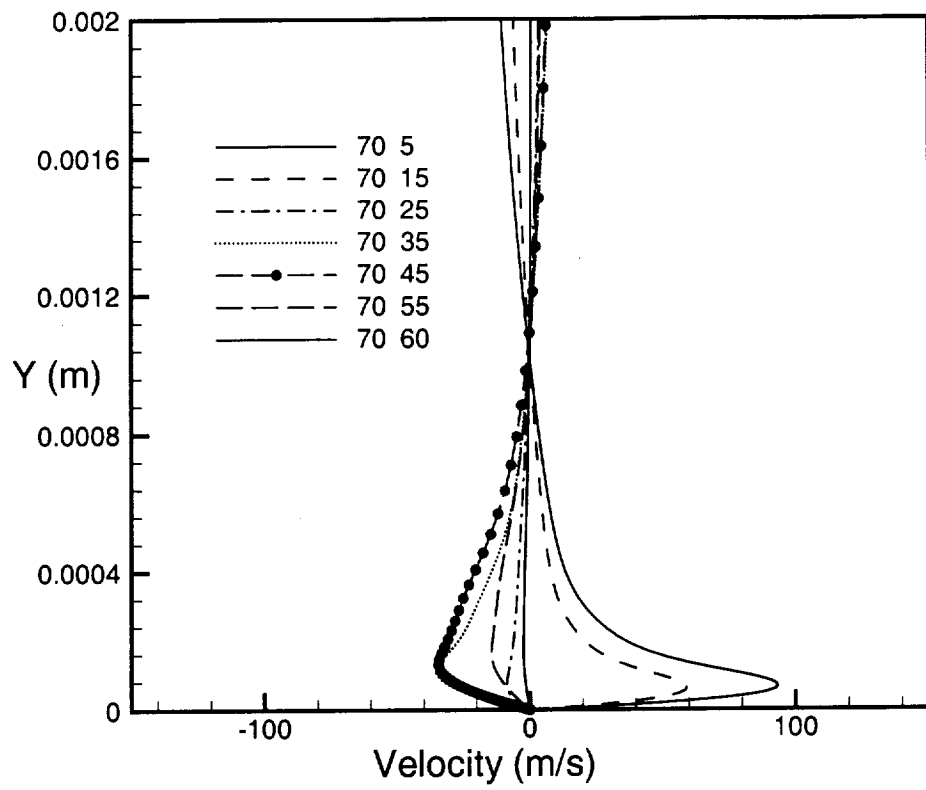


Figure 13. Boundary layer crossflow velocity profiles $I=70$.

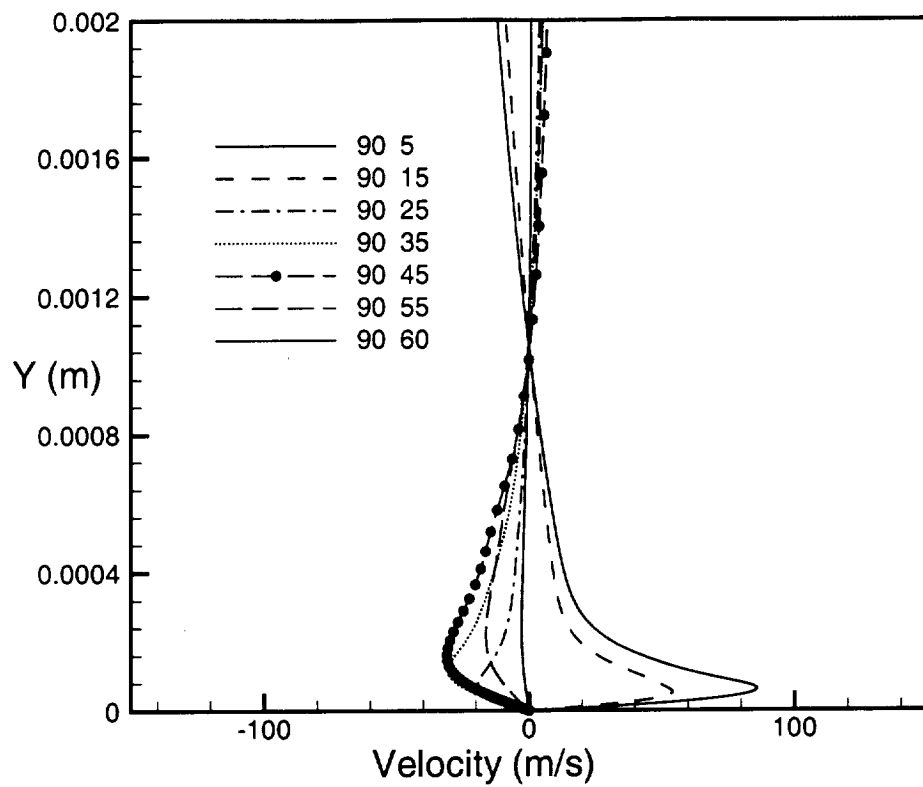


Figure 14. Boundary layer crossflow velocity profiles $I=90$.

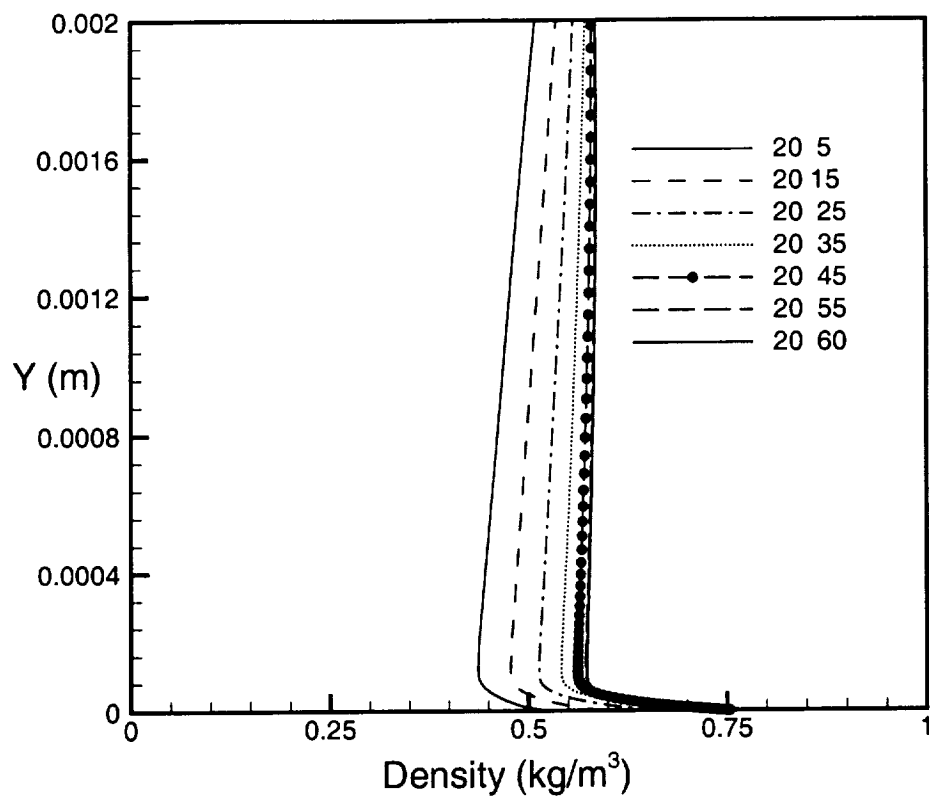


Figure 15. Boundary layer density profiles $I=20$.

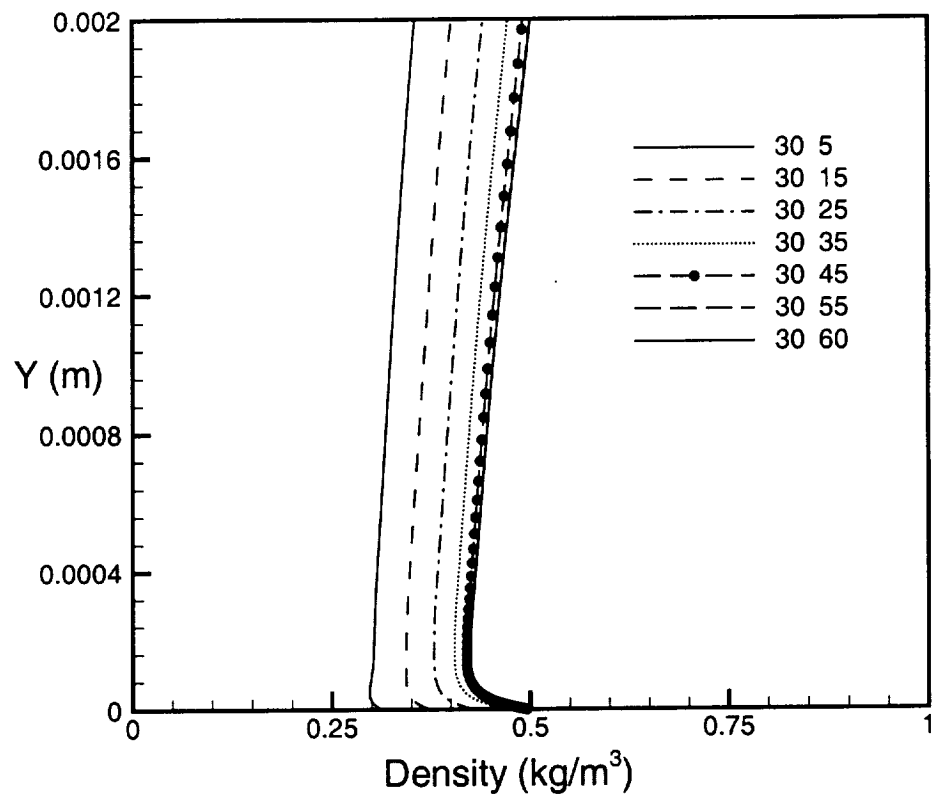


Figure 16. Boundary layer density profiles $I=30$.

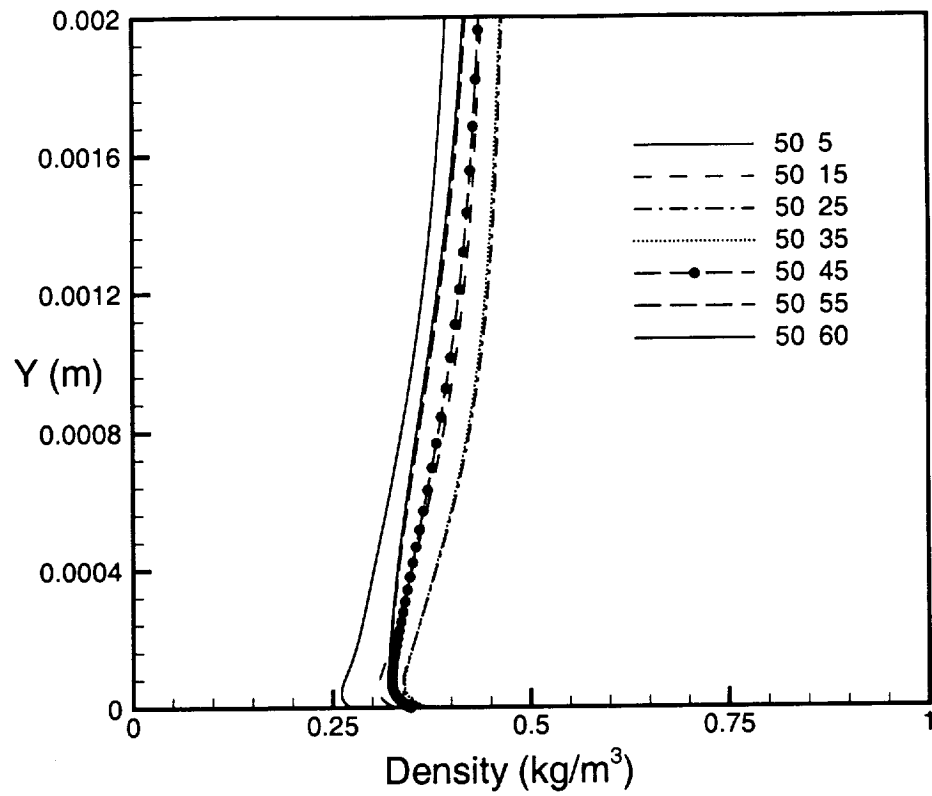


Figure 17. Boundary layer density profiles I=50.

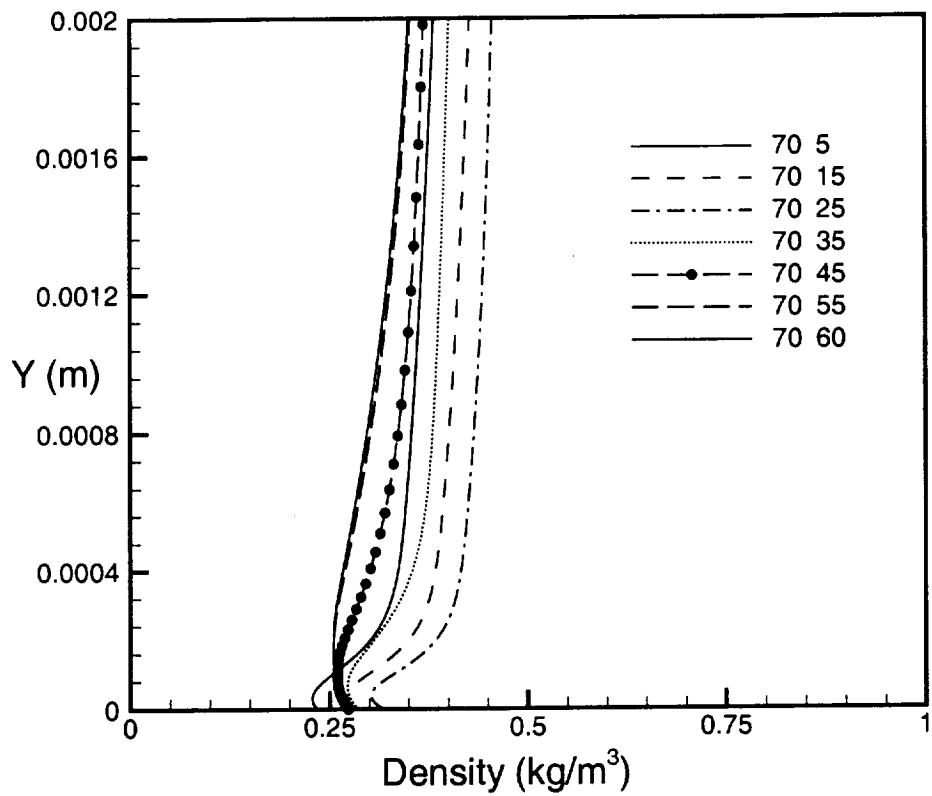


Figure 18. Boundary layer density profiles $I=70$.

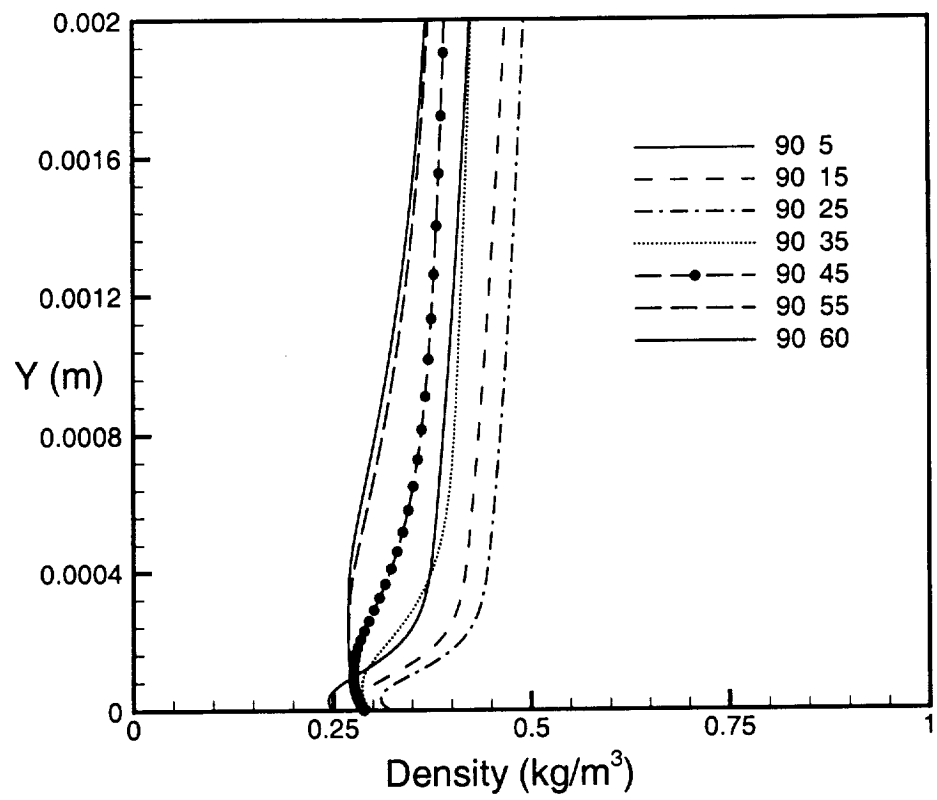


Figure 19. Boundary layer density profiles I=90.

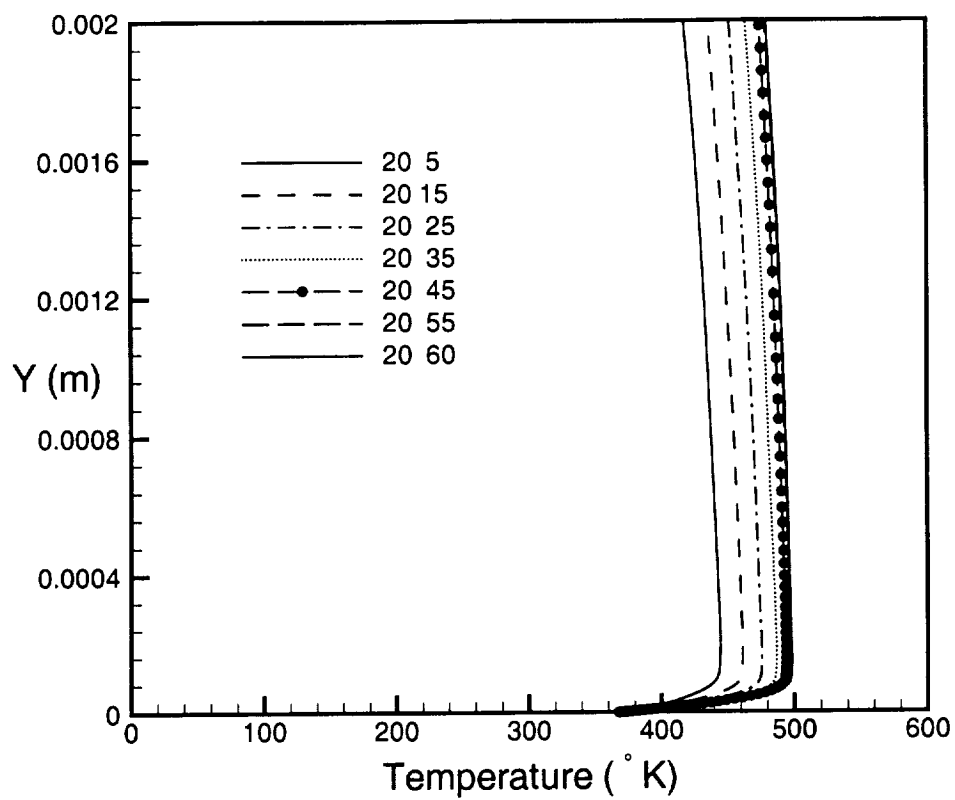


Figure 20. Boundary layer temperature profiles I=20.

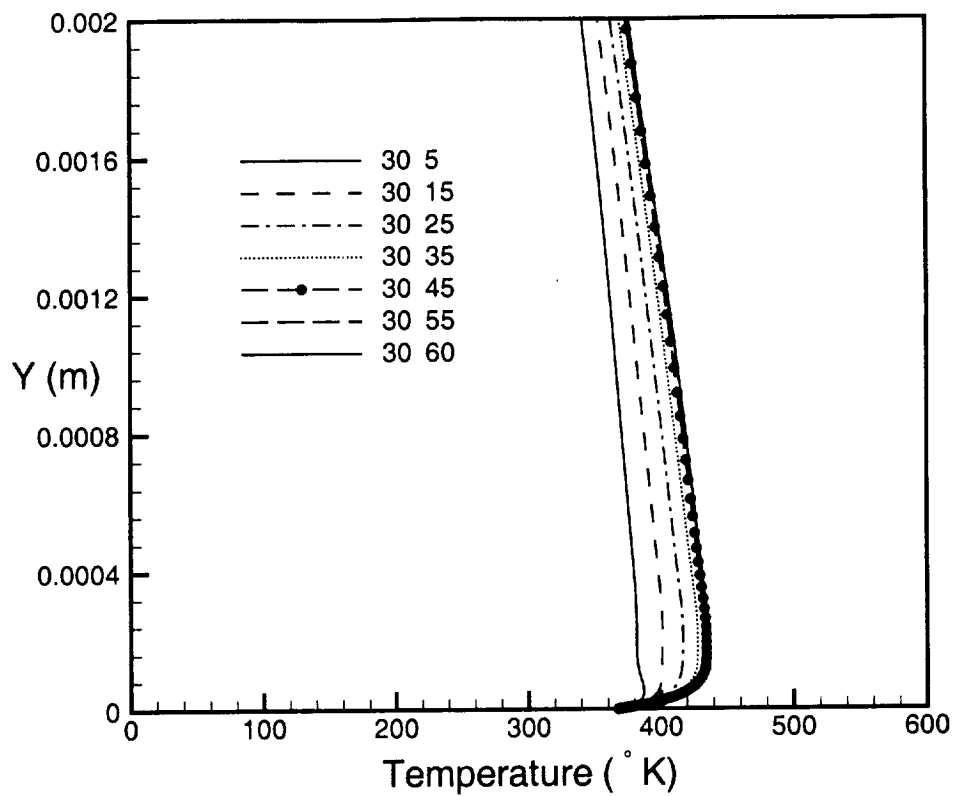


Figure 21. Boundary layer temperature profiles $I=30$.

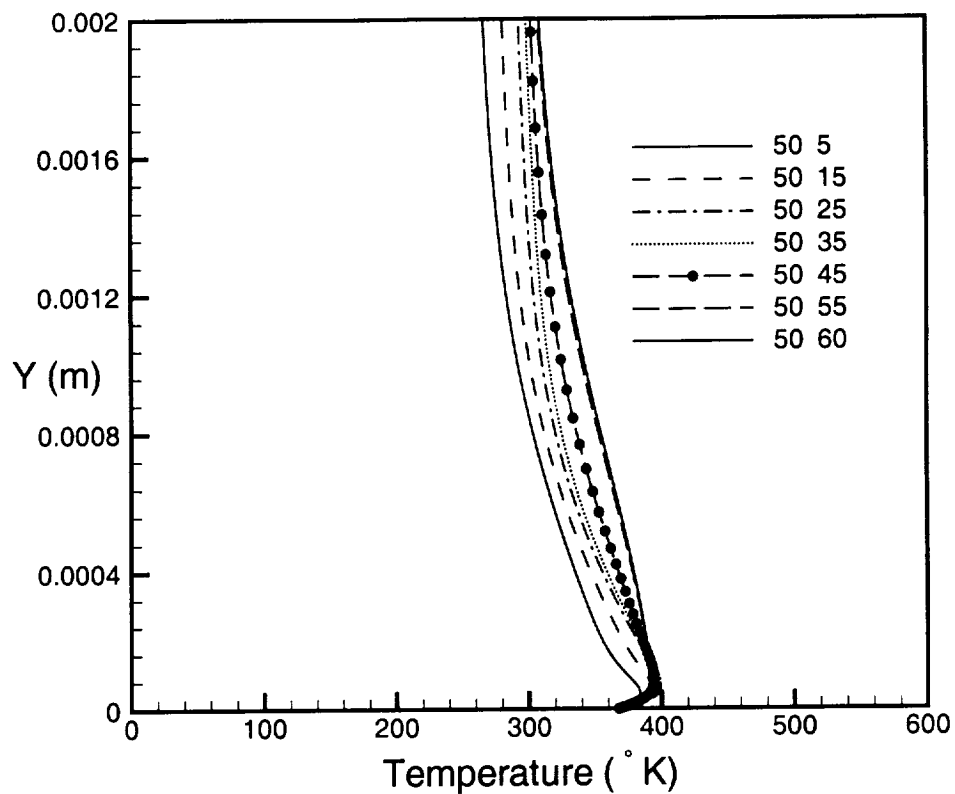


Figure 22. Boundary layer temperature profiles I=50.

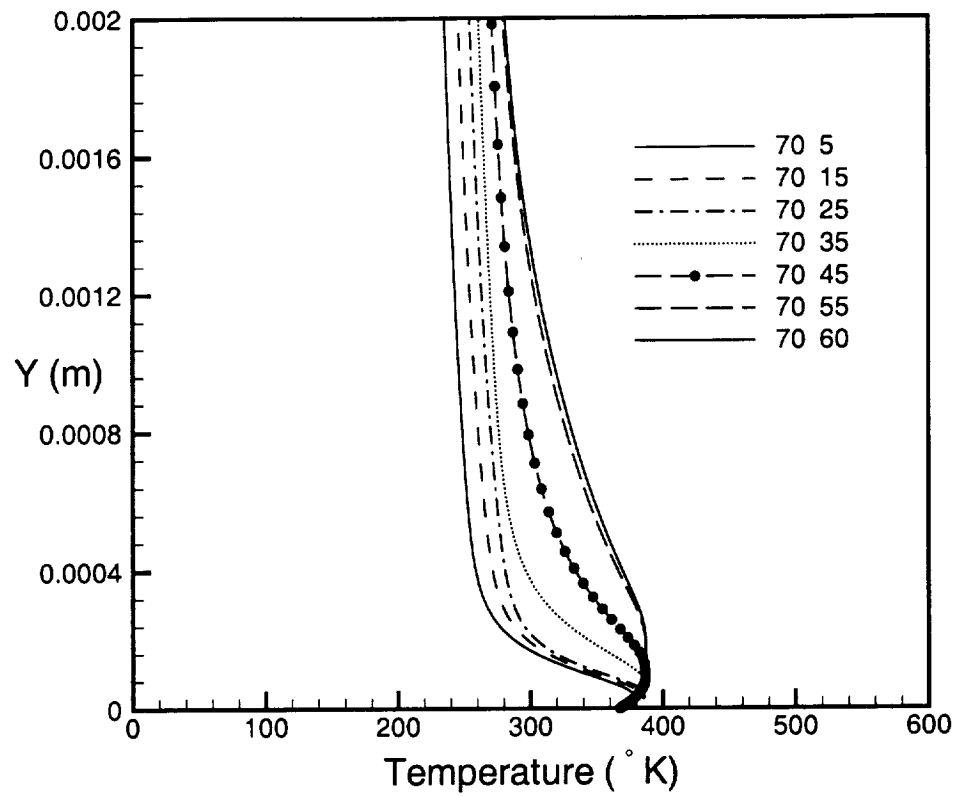


Figure 23. Boundary layer temperature profiles $I=70$.

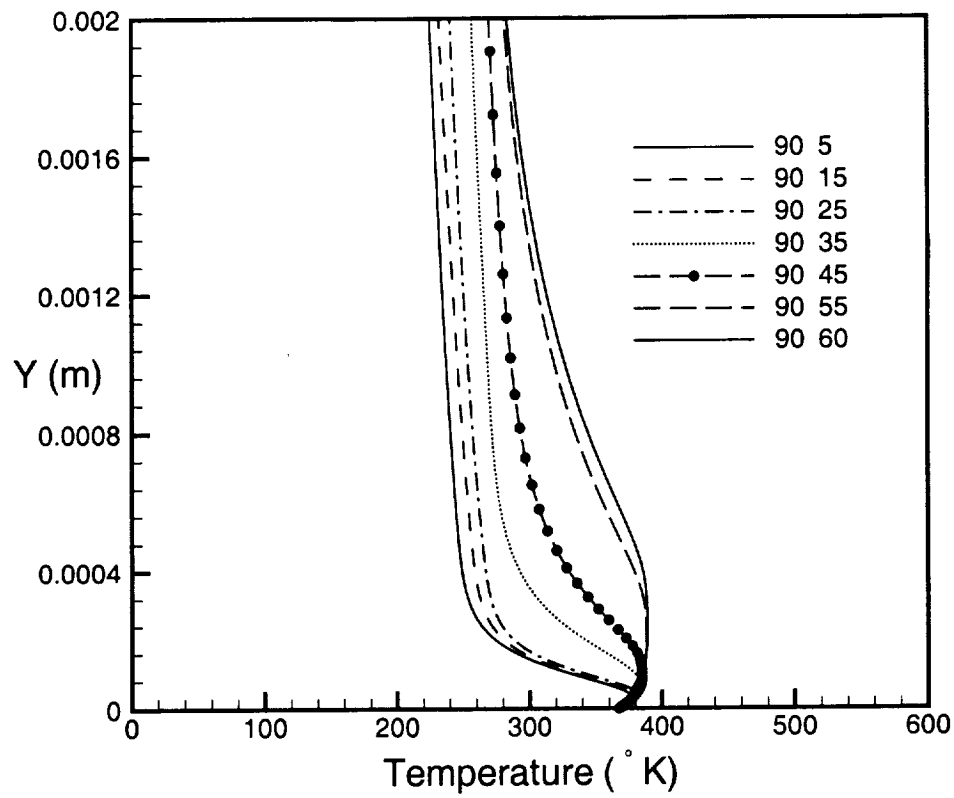


Figure 24. Boundary layer temperature profiles $I=90$.

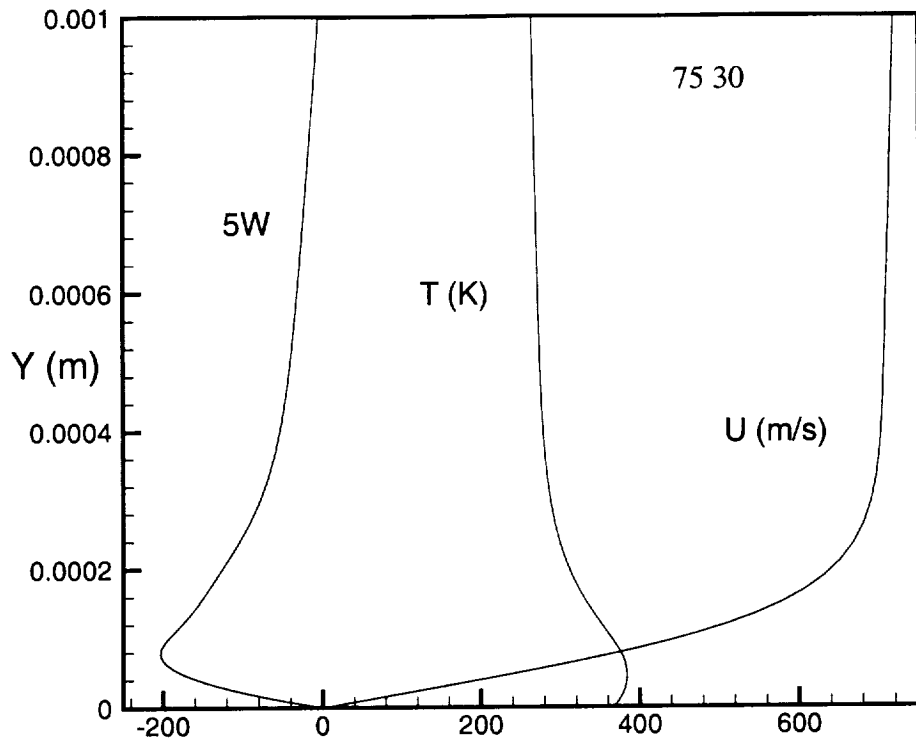


Figure 25. Boundary layer profiles $I=75$ $J=30$.

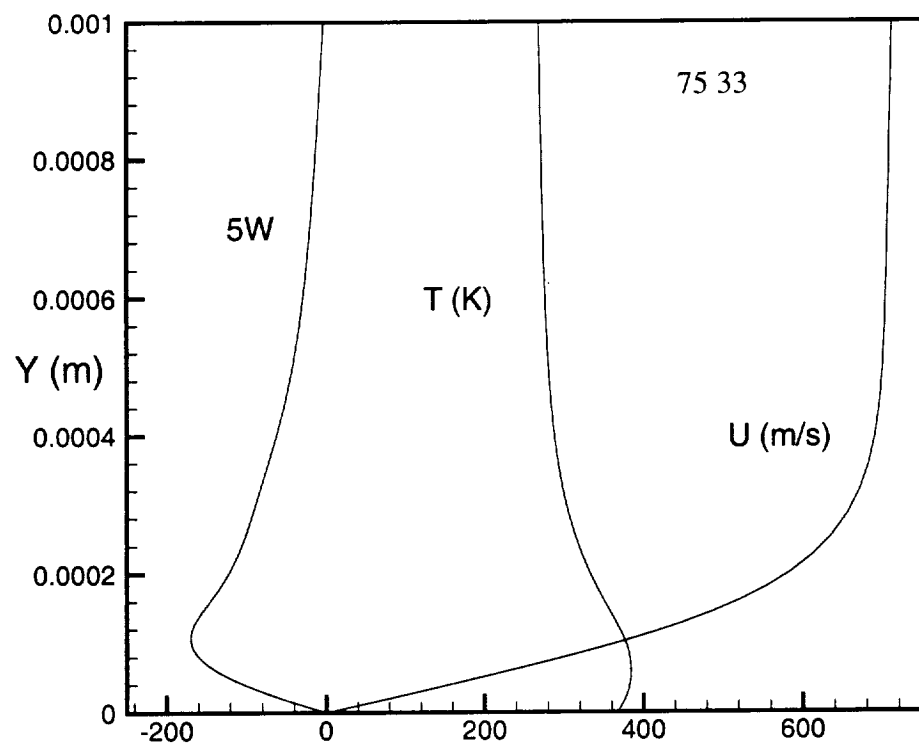


Figure 26. Boundary layer profiles $I=75$ $J=33$.

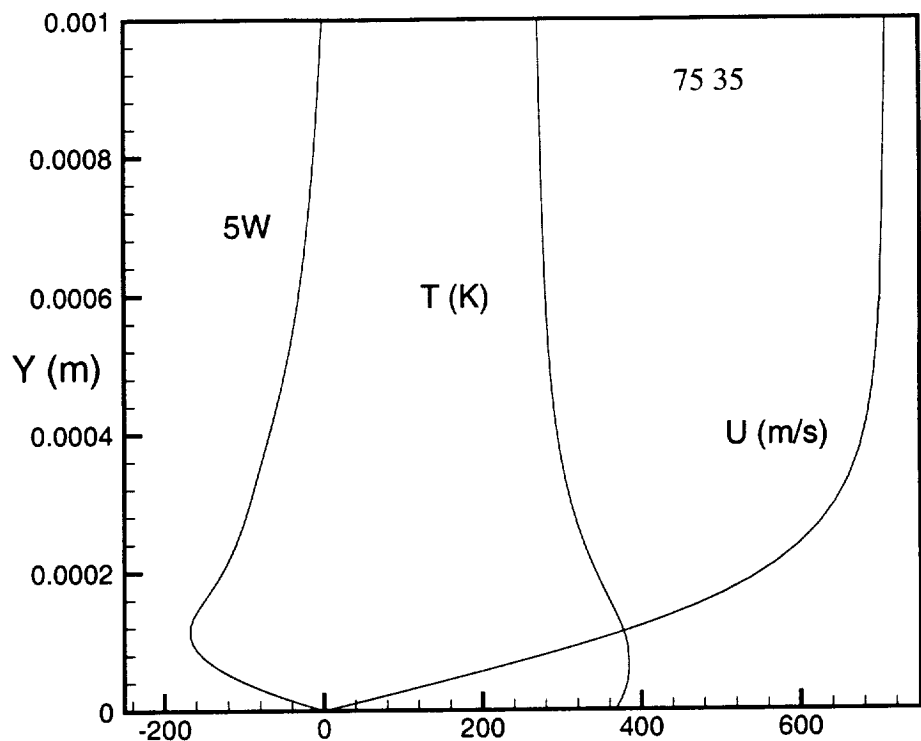


Figure 27. Boundary layer profiles $I=75$ $J=35$.

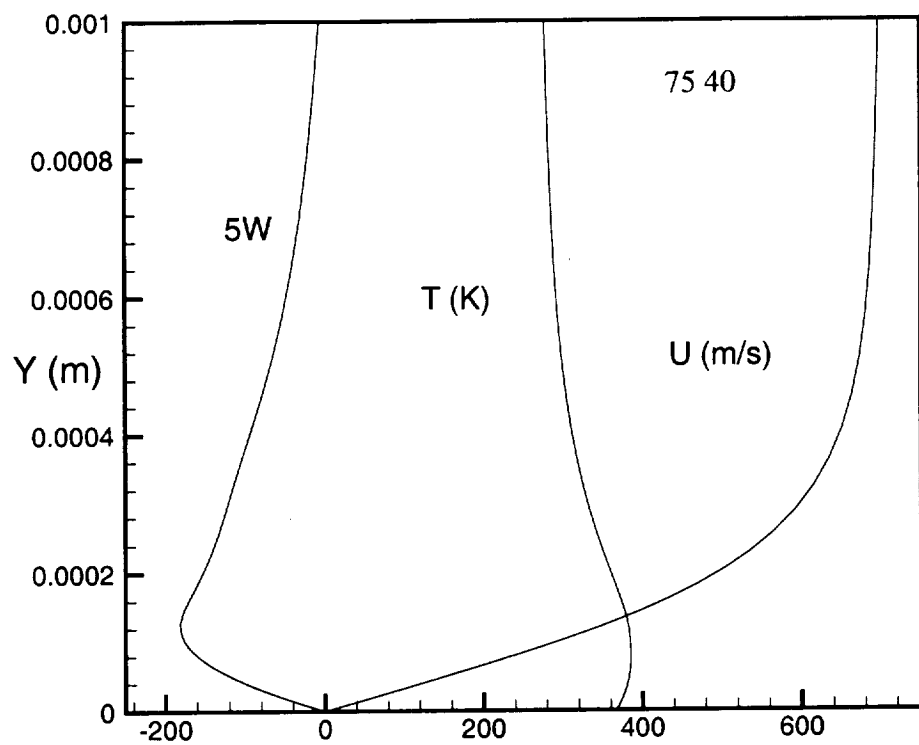


Figure 28. Boundary layer profiles $I=75$ $J=40$.

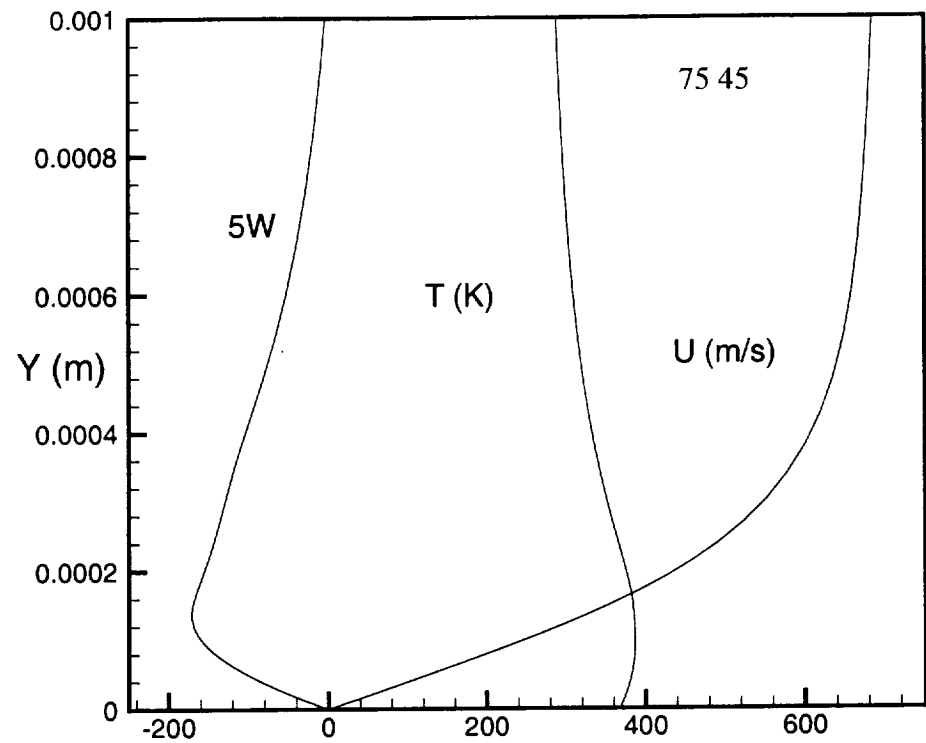


Figure 29. Boundary layer profiles $I=75$ $J=45$.

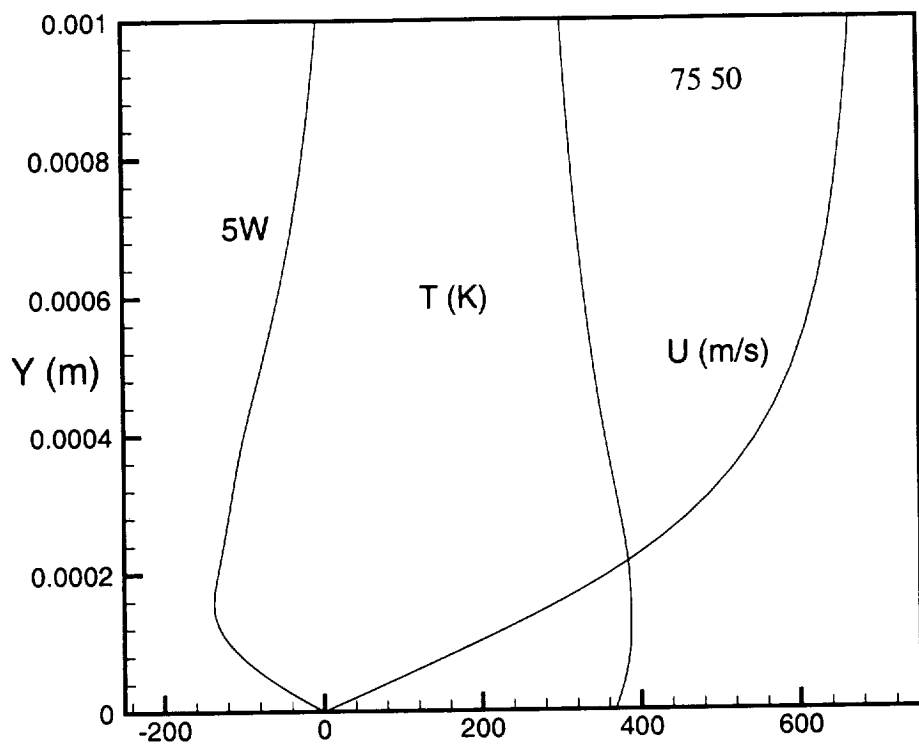


Figure 27. Boundary layer profiles $I=75$ $J=50$.

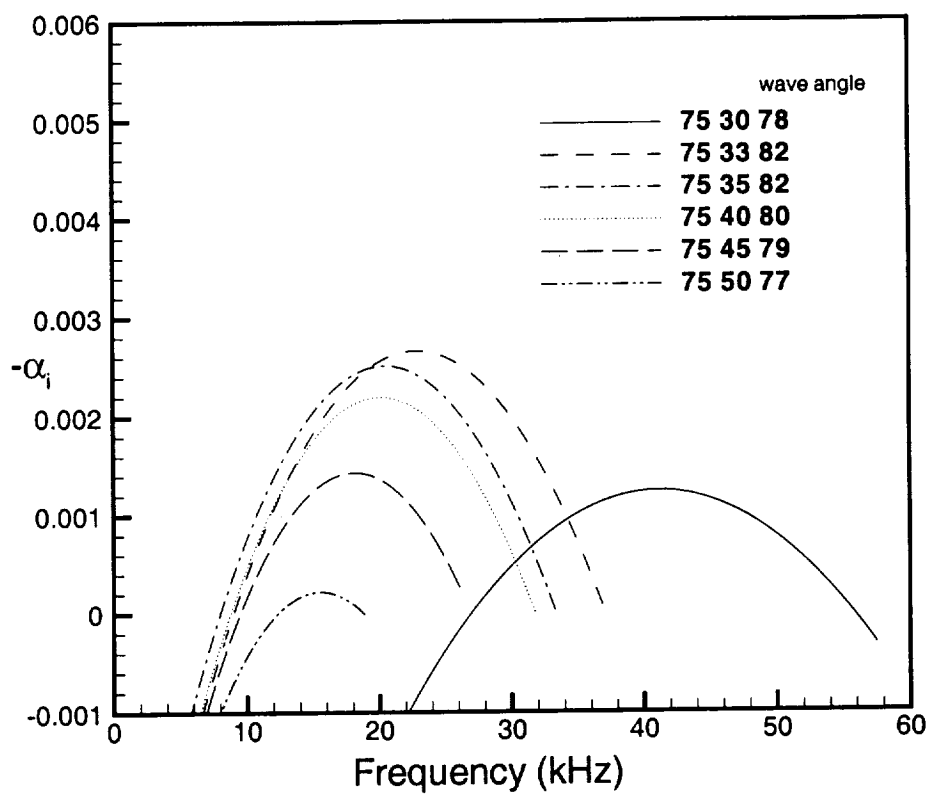


Figure 31. Growth rates from linear stability computations at $I=75$.

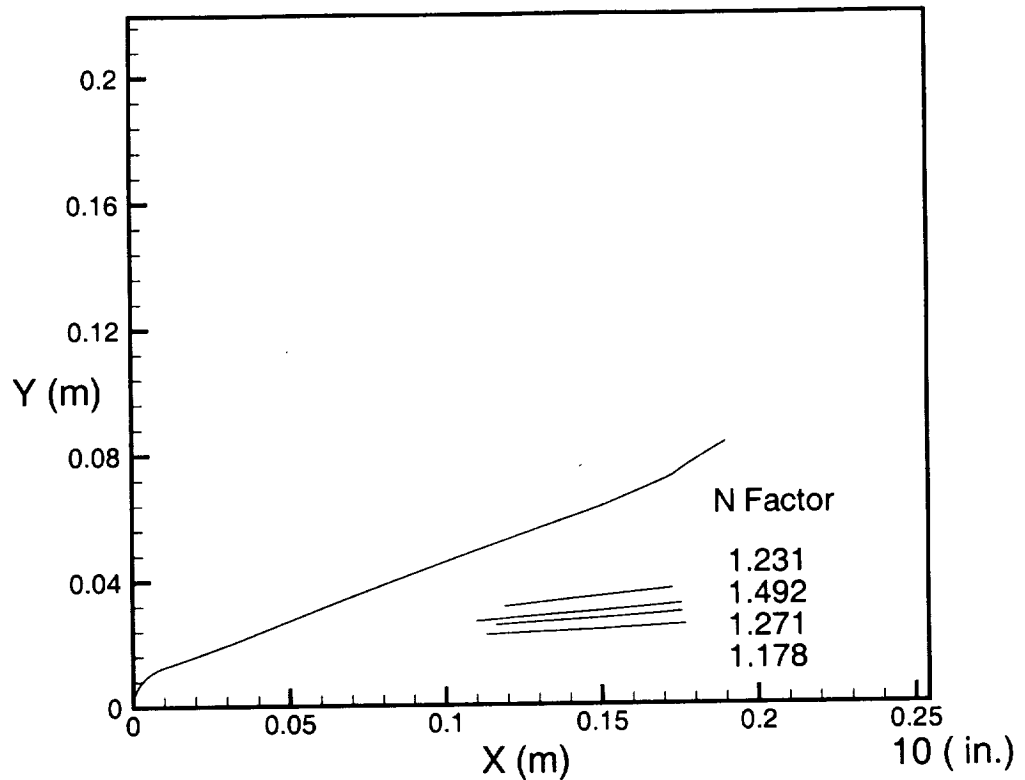


Figure 32. N - Factor traces for case 1.

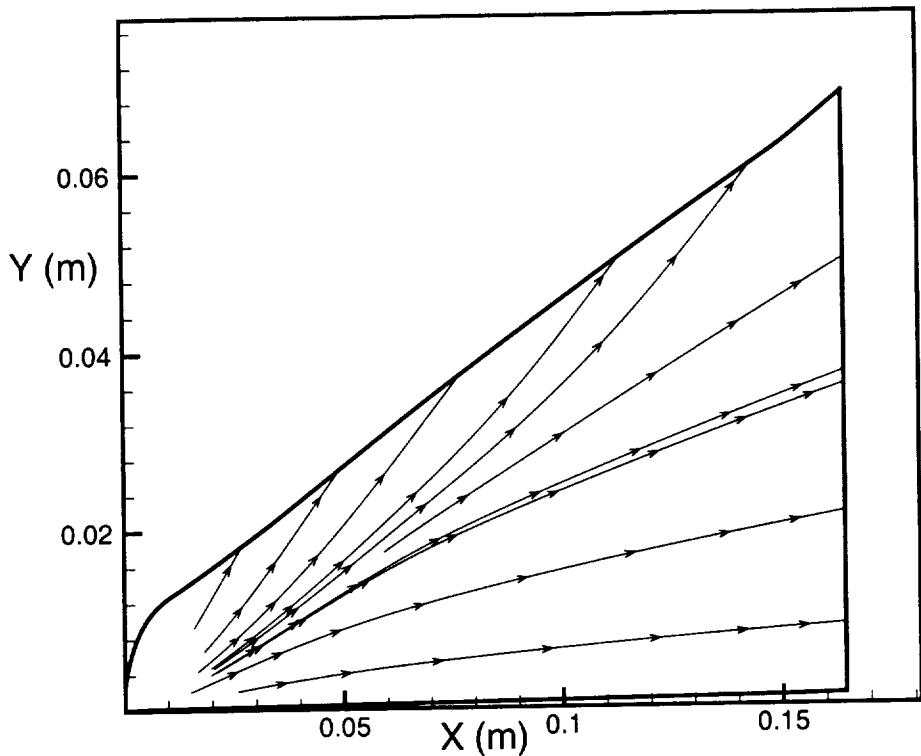


Figure 33. Streamlines pattern Case 2.

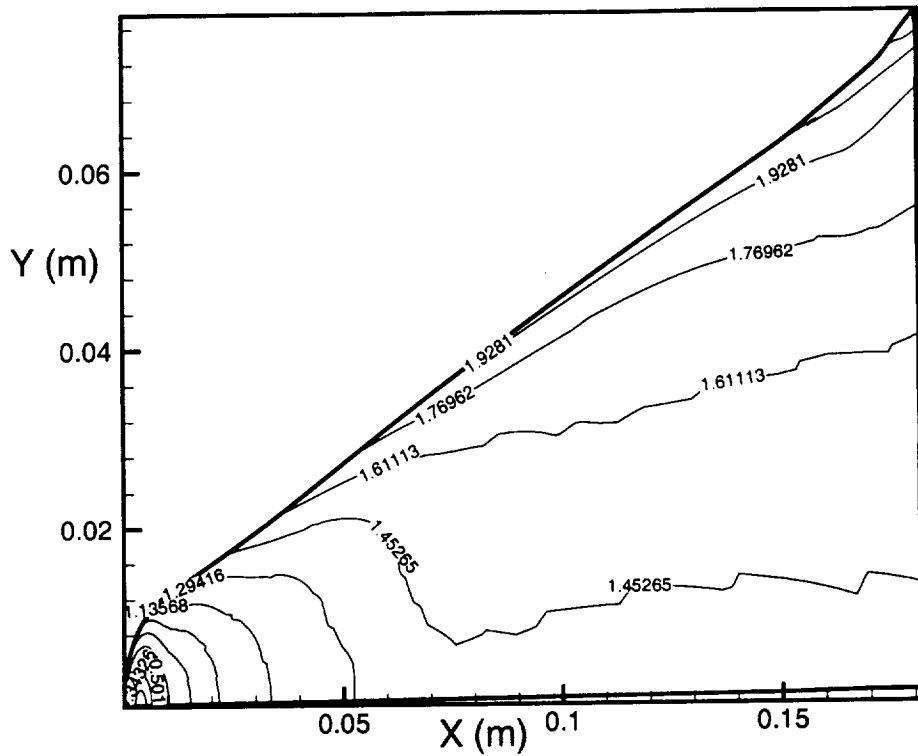


Figure 34. Mach contours Case 2.

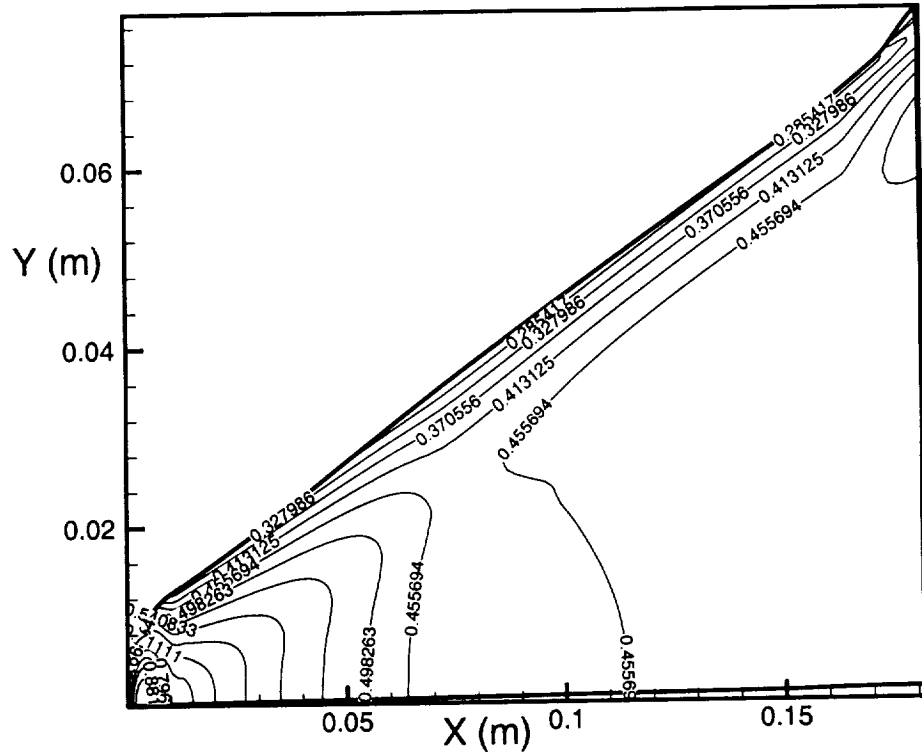


Figure 3. Pressure contours.

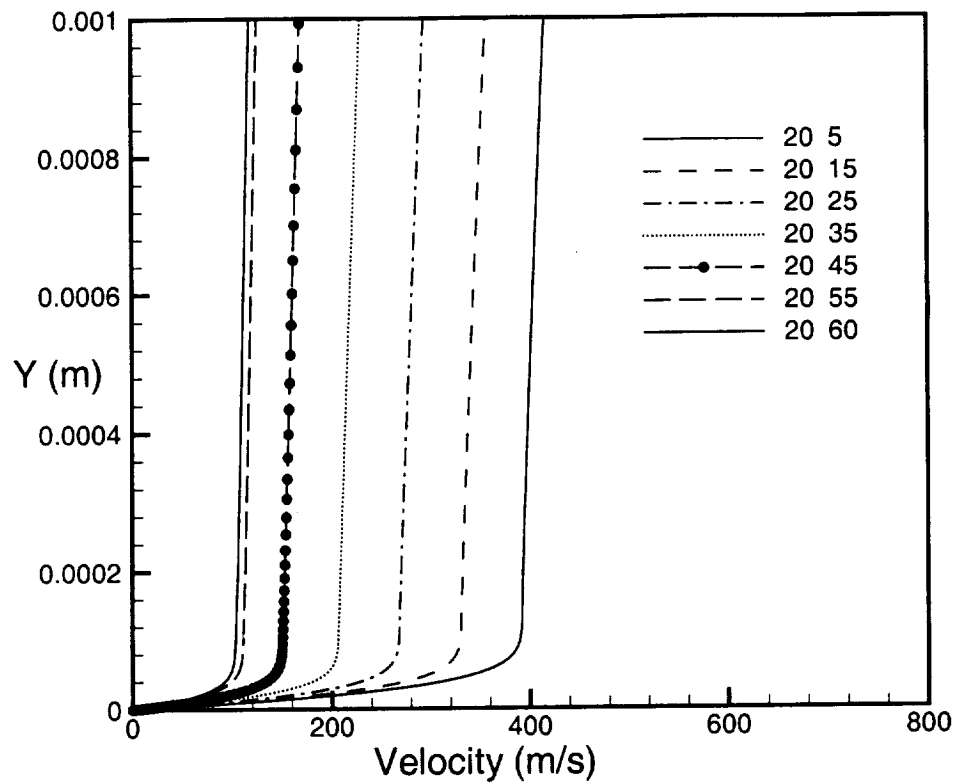


Figure 36. Boundary layer velocity profiles along the inviscid streamlines $I=20$.

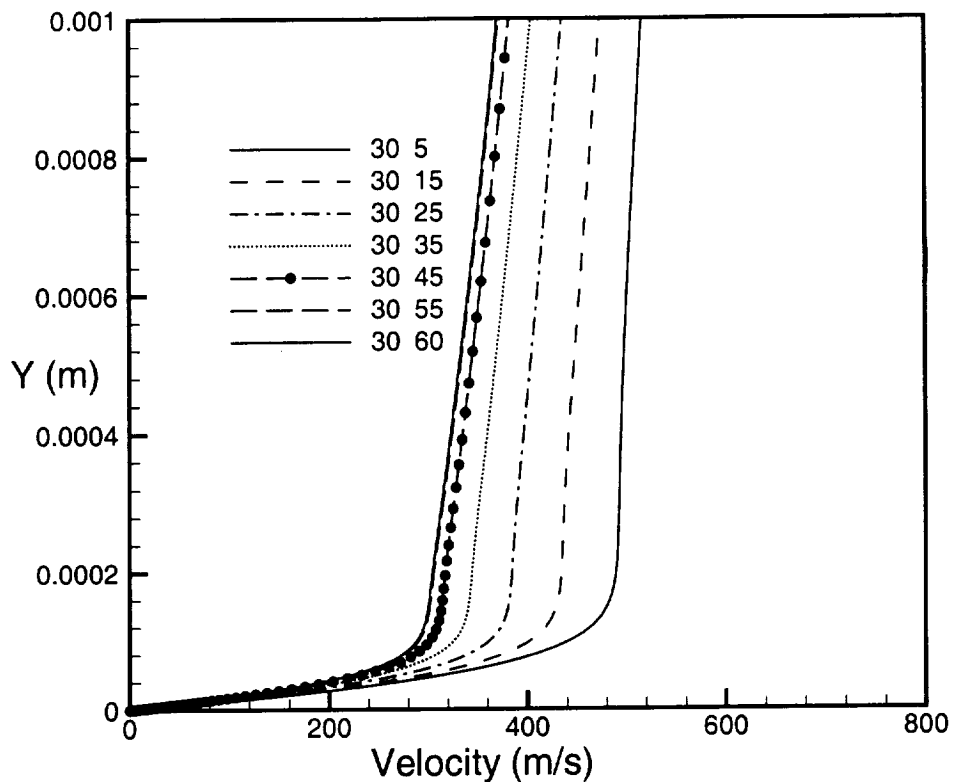


Figure 37. Boundary layer velocity profiles along the inviscid streamlines $I=30$.

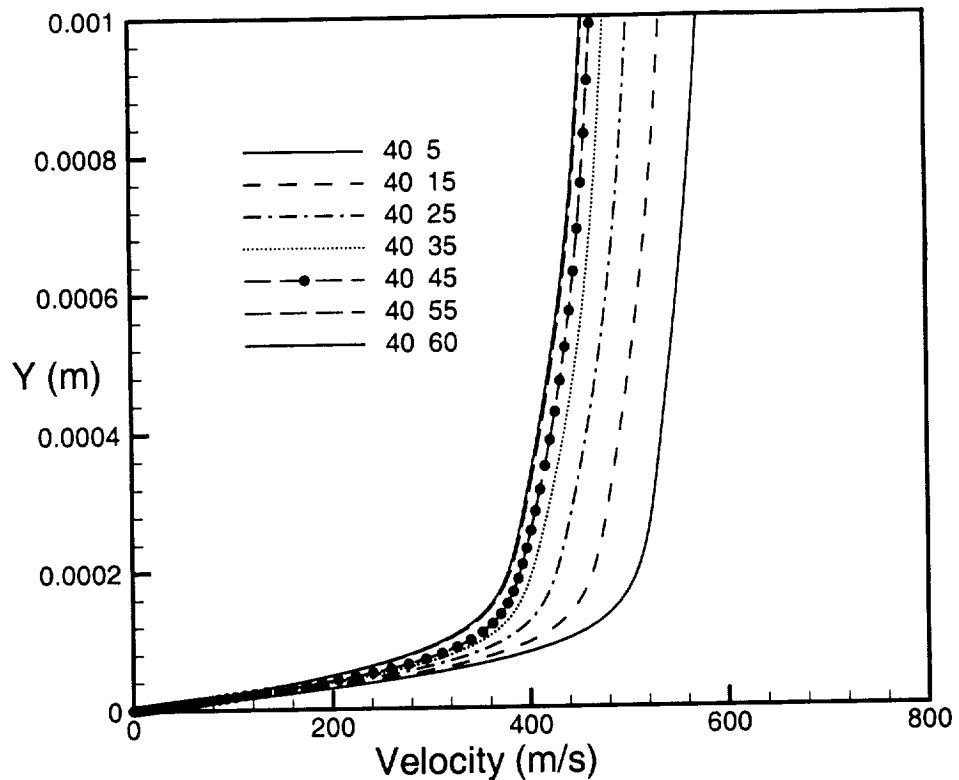


Figure 38. Boundary layer velocity profiles along the inviscid streamlines $I=40$.

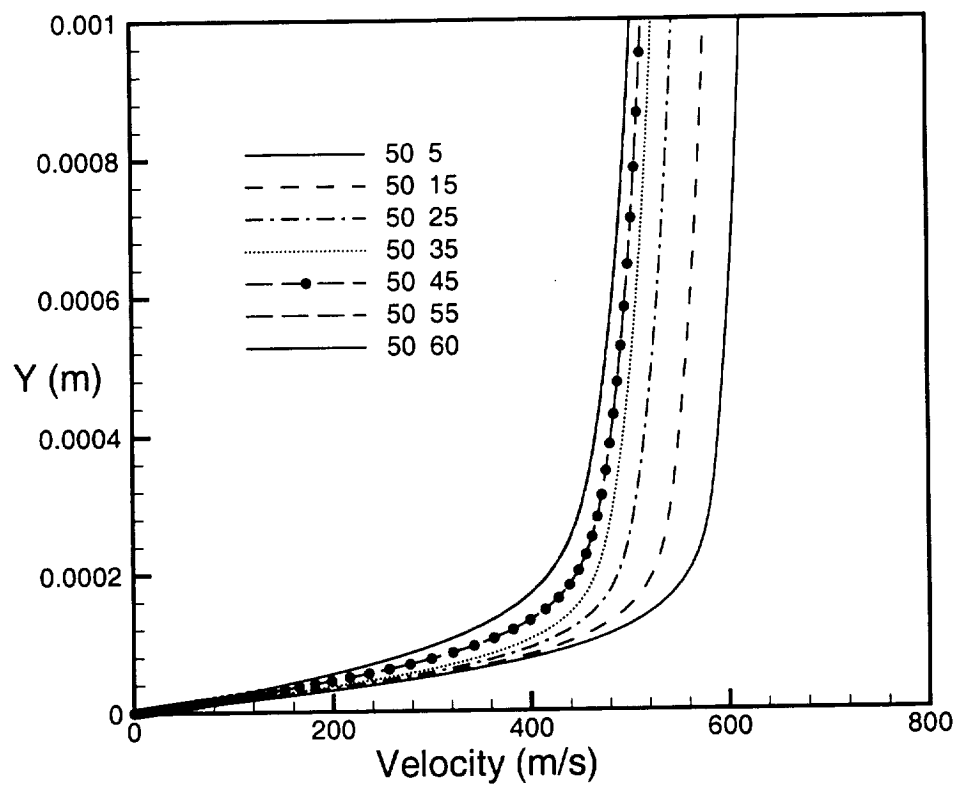


Figure 39. Boundary layer velocity profiles along the inviscid streamlines $I=50$.

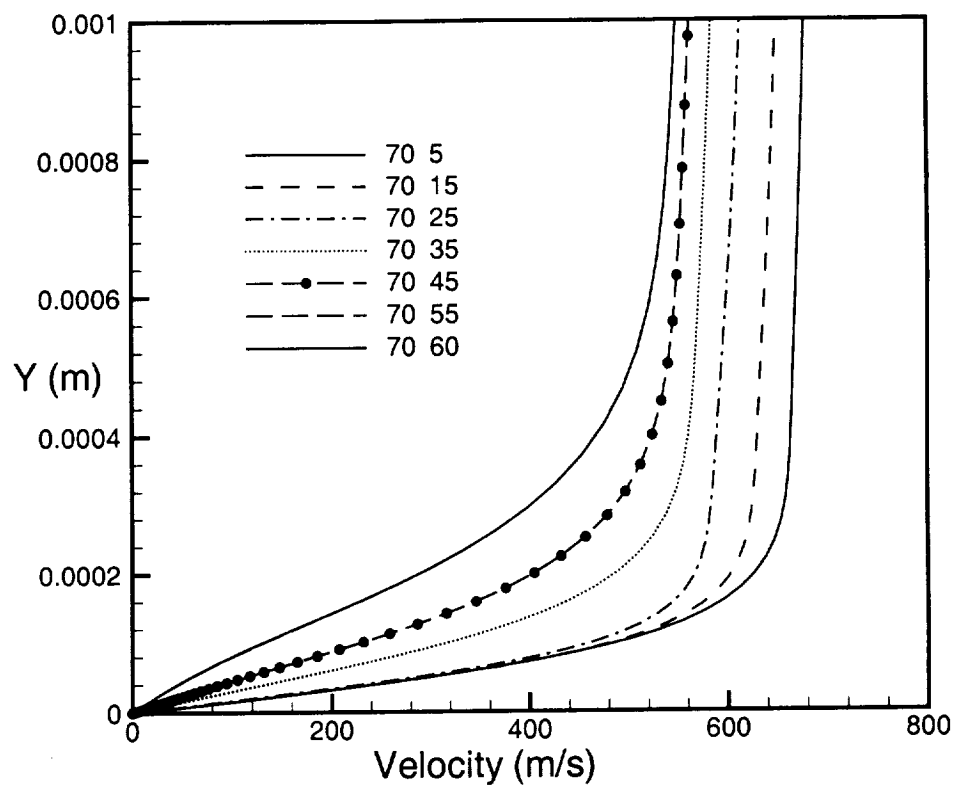


Figure 40. Boundary layer velocity profiles along the inviscid streamlines $I=70$.

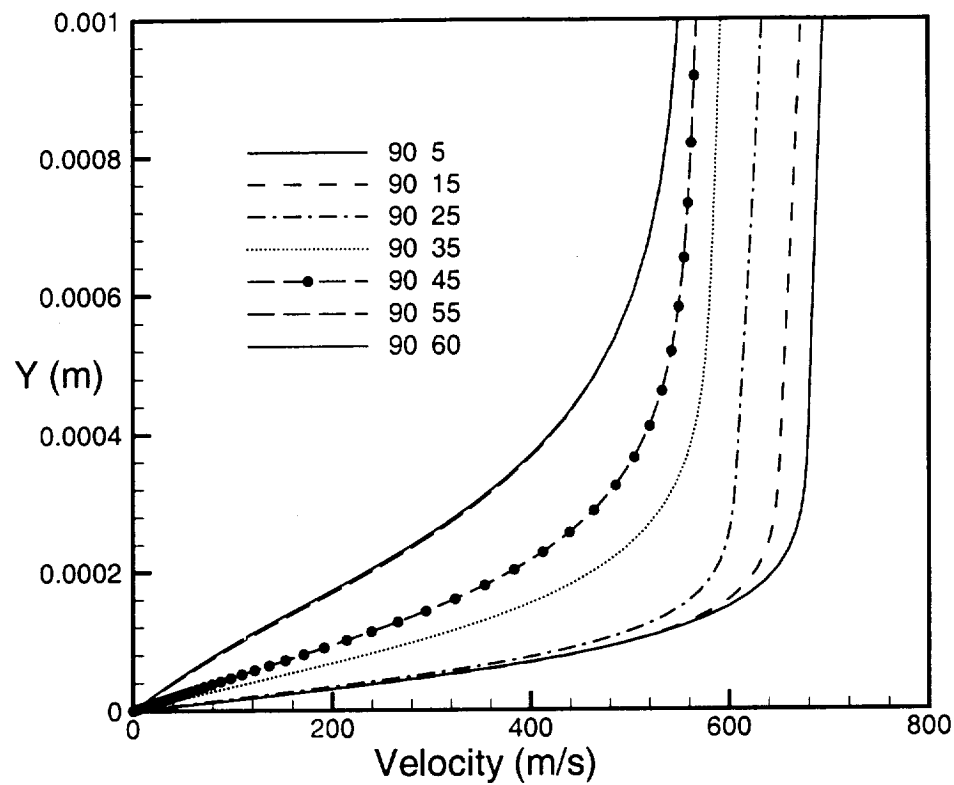


Figure 41. Boundary layer velocity profiles along the inviscid streamlines I=90.

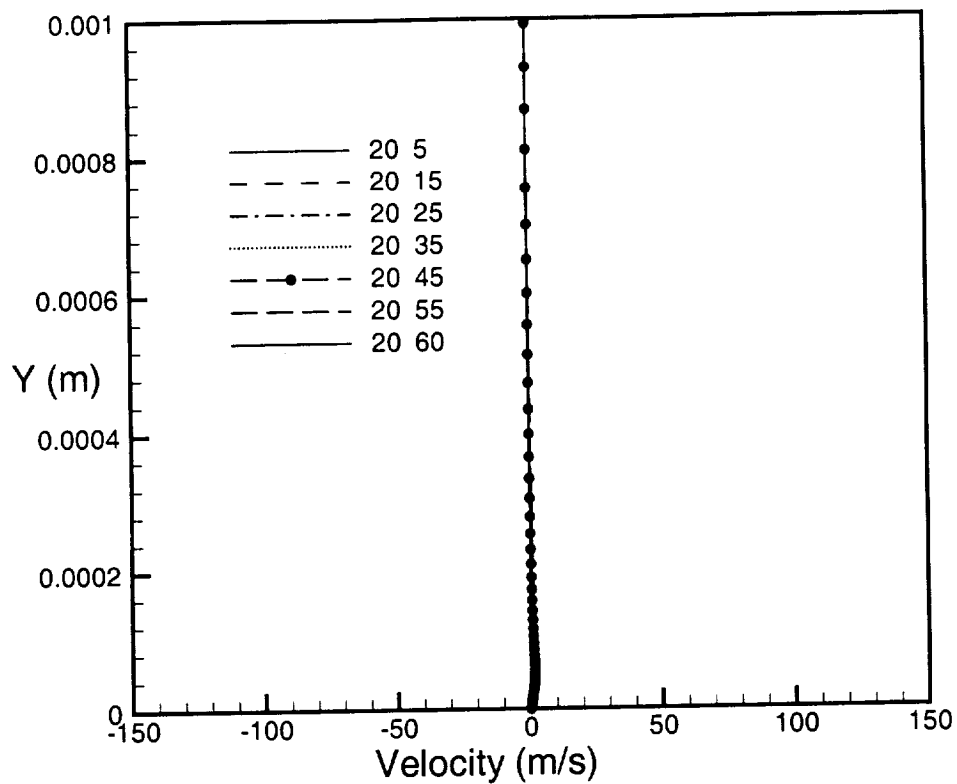


Figure 42. Boundary layer crossflow velocity profiles $I=20$.

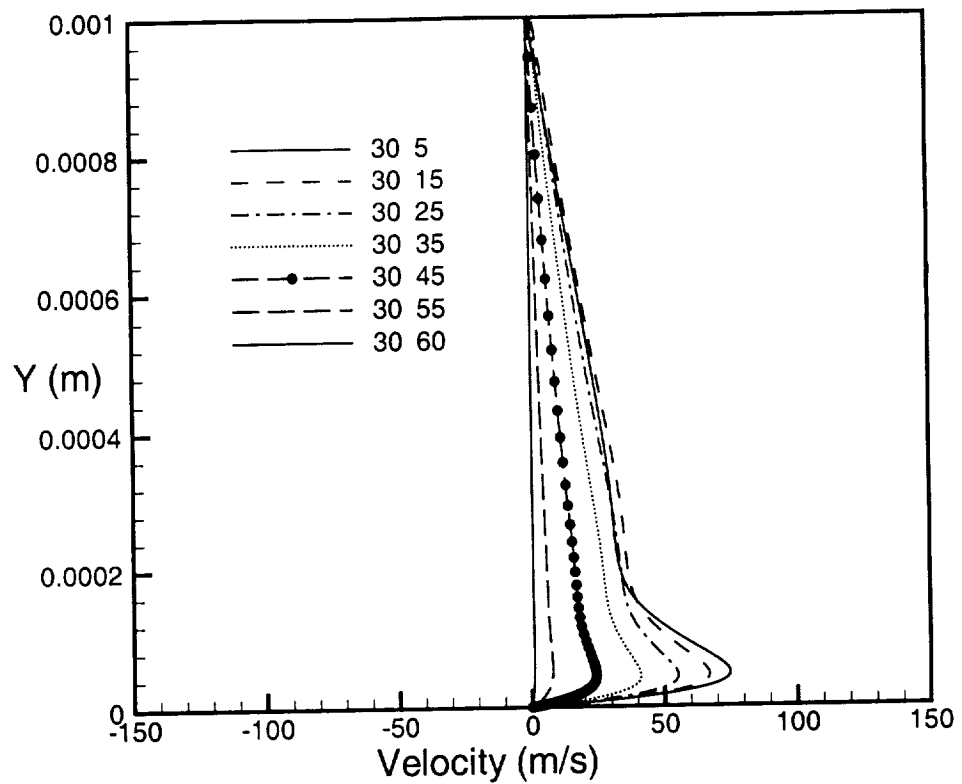


Figure 43. Boundary layer crossflow velocity profiles I=30.

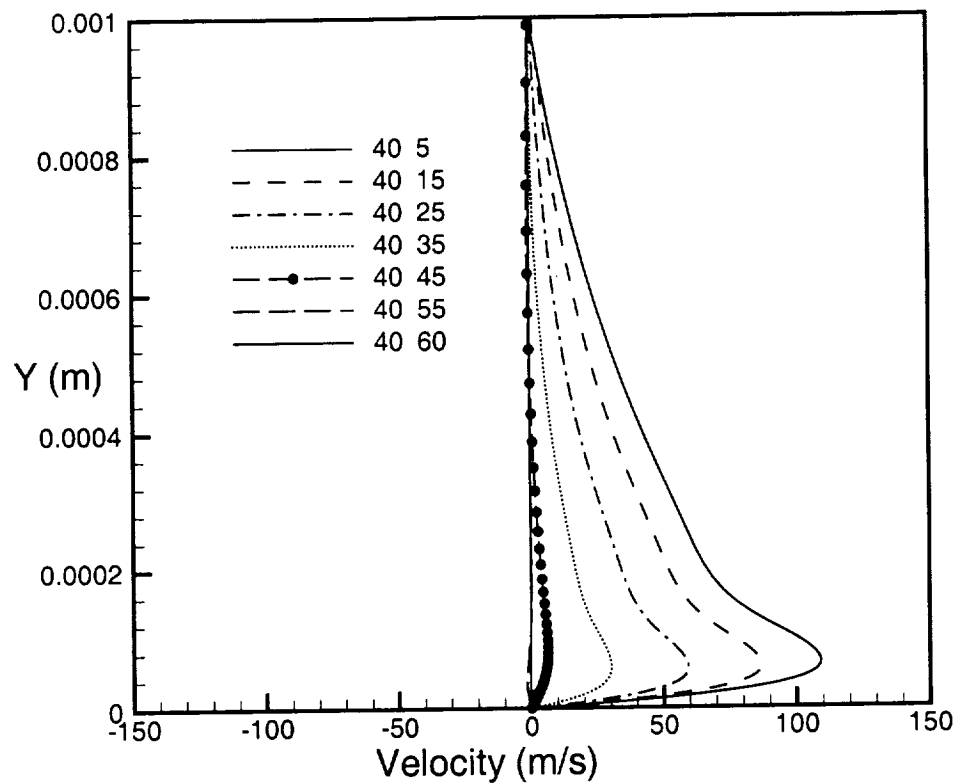


Figure 44. Boundary layer crossflow velocity profiles $I=40$.

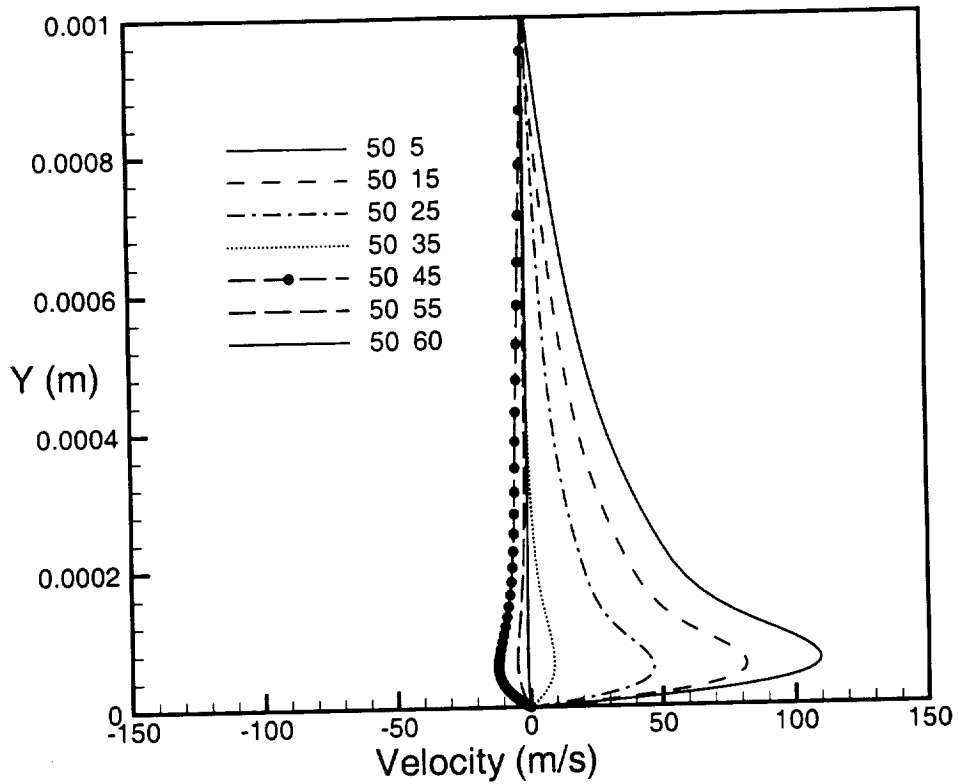


Figure 45. Boundary layer crossflow velocity profiles $I=50$.

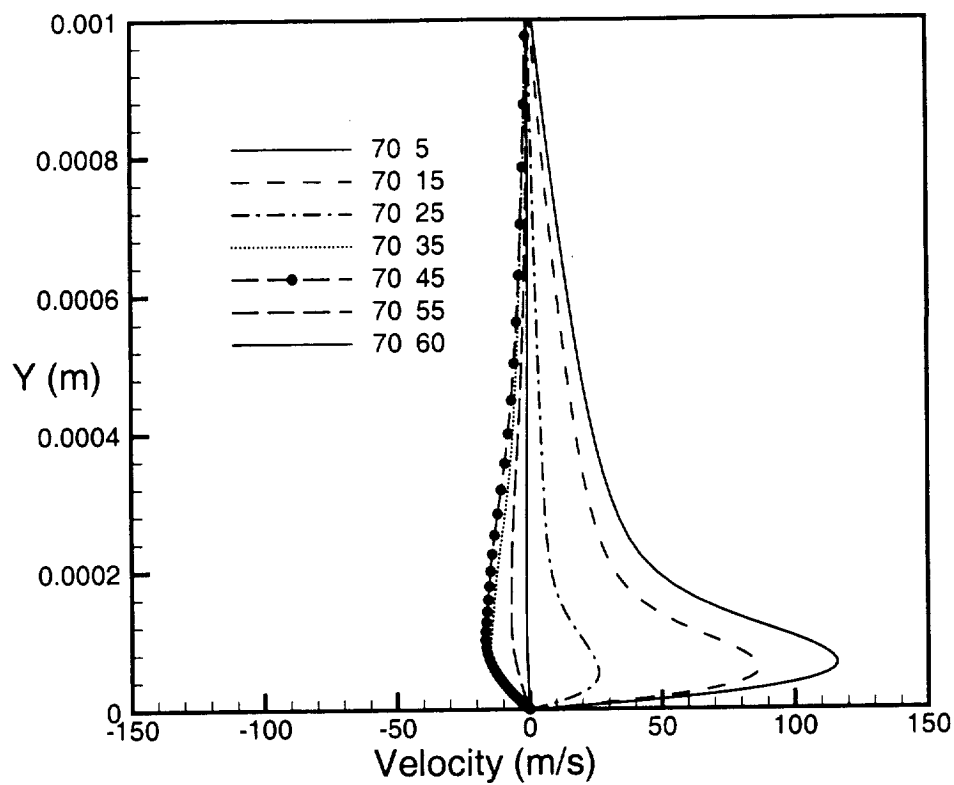


Figure 46. Boundary layer crossflow velocity profiles I=70.

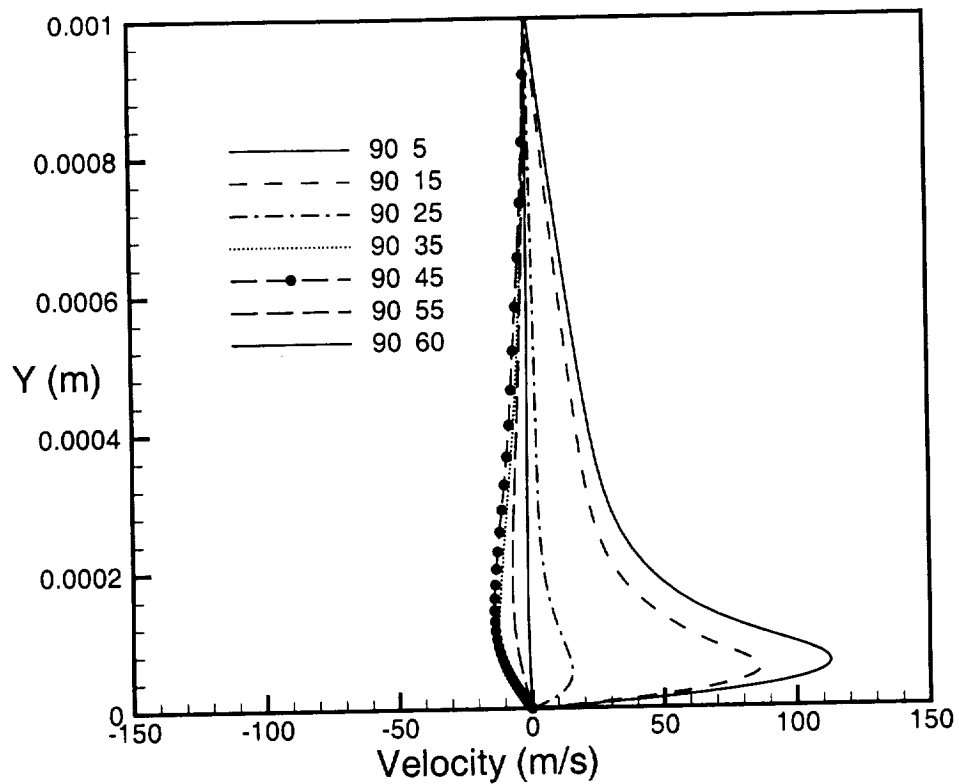


Figure 47. Boundary layer crossflow velocity profiles $I=90$.

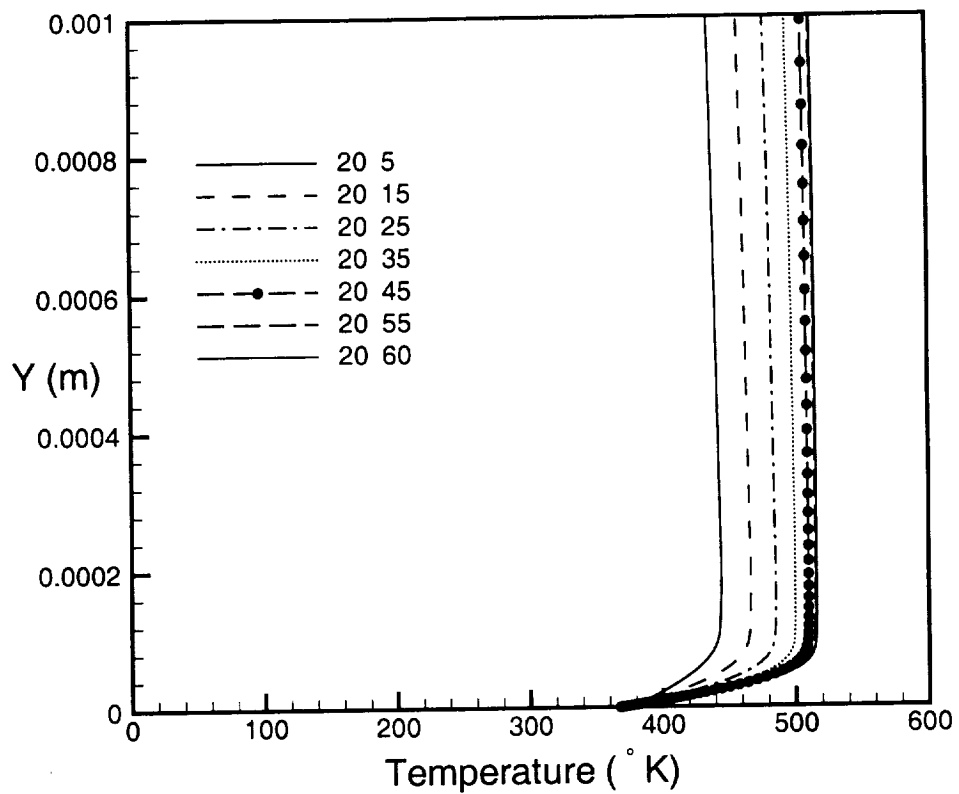


Figure 48. Boundary layer temperature profiles $I=20$.

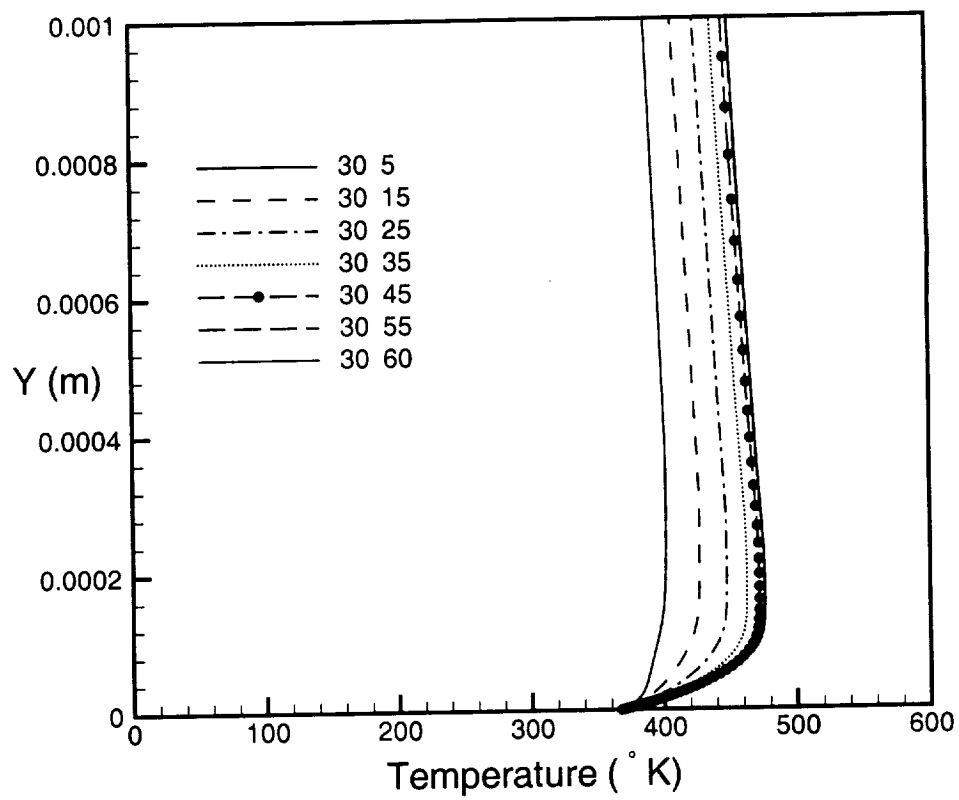


Figure 49. Boundary layer temperature profiles I=30.

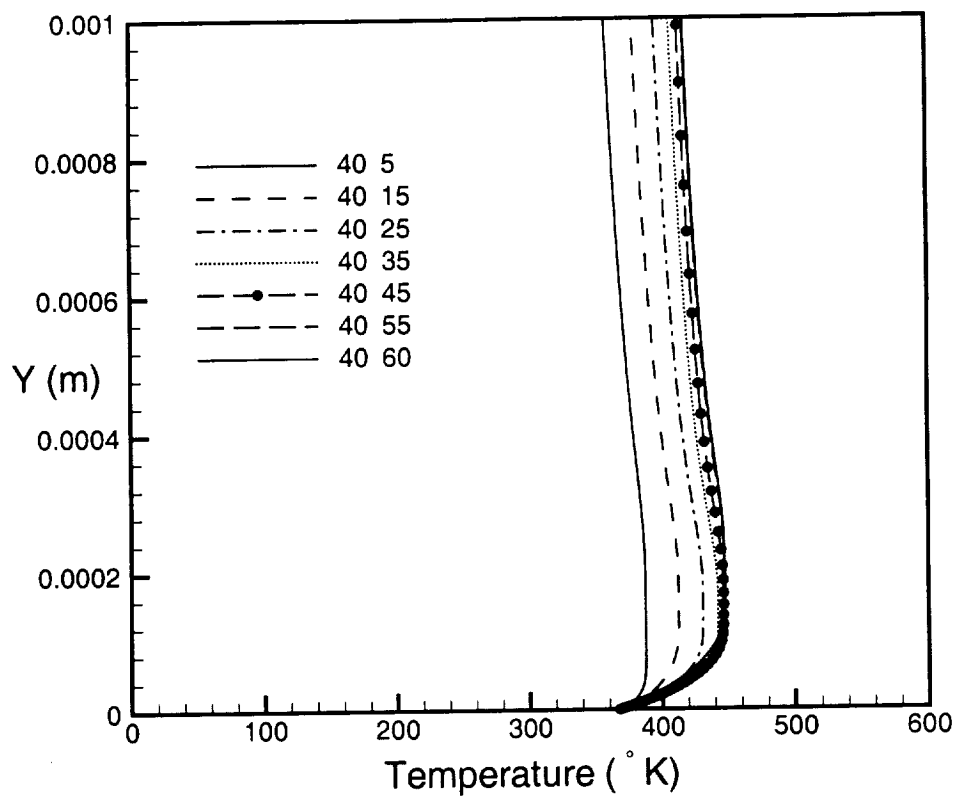


Figure 50. Boundary layer temperature profiles $I=40$.

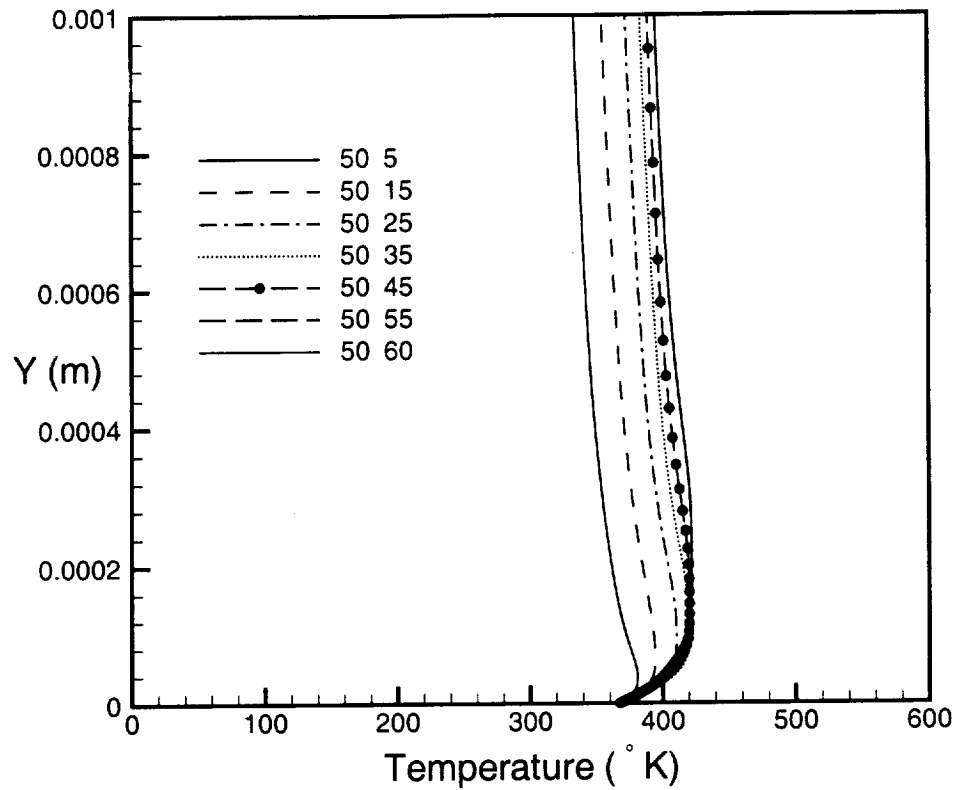


Figure 51. Boundary layer temperature profiles $I=50$.

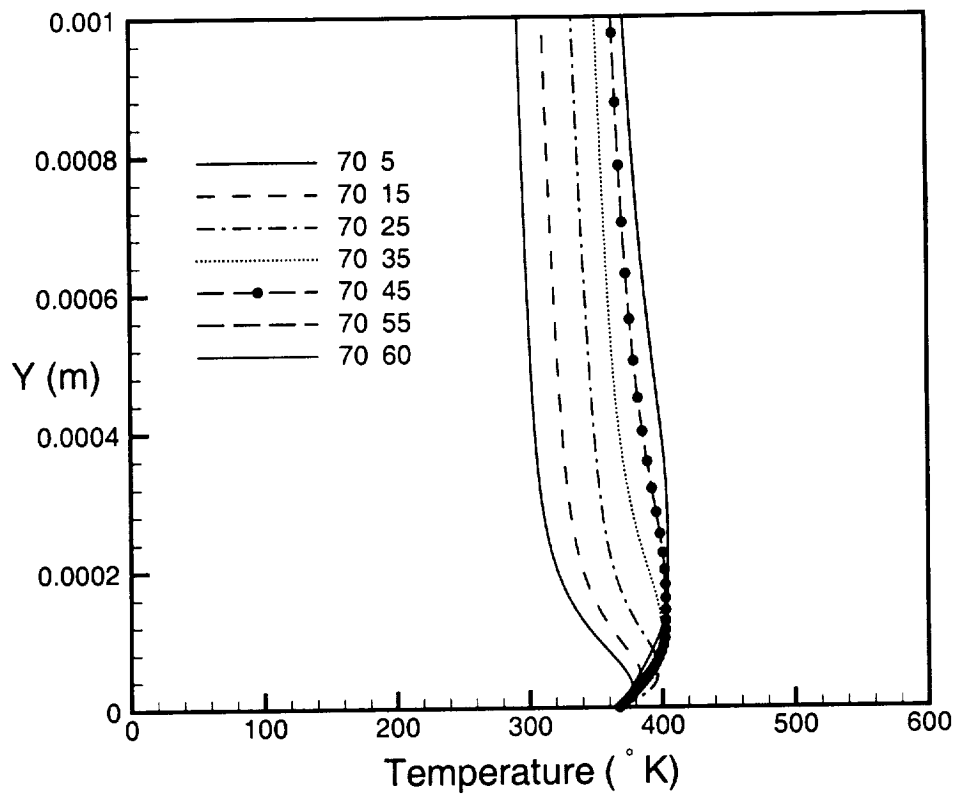


Figure 52. Boundary layer temperature profiles $I=70$.

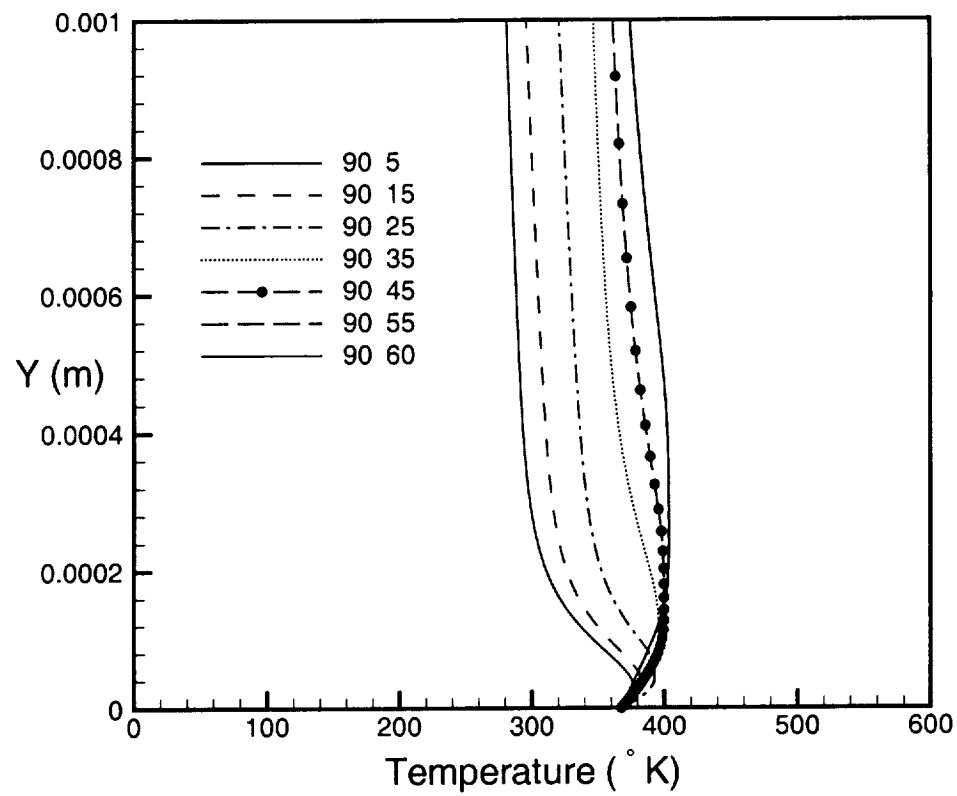


Figure 53. Boundary layer temperature profiles $I=90$.

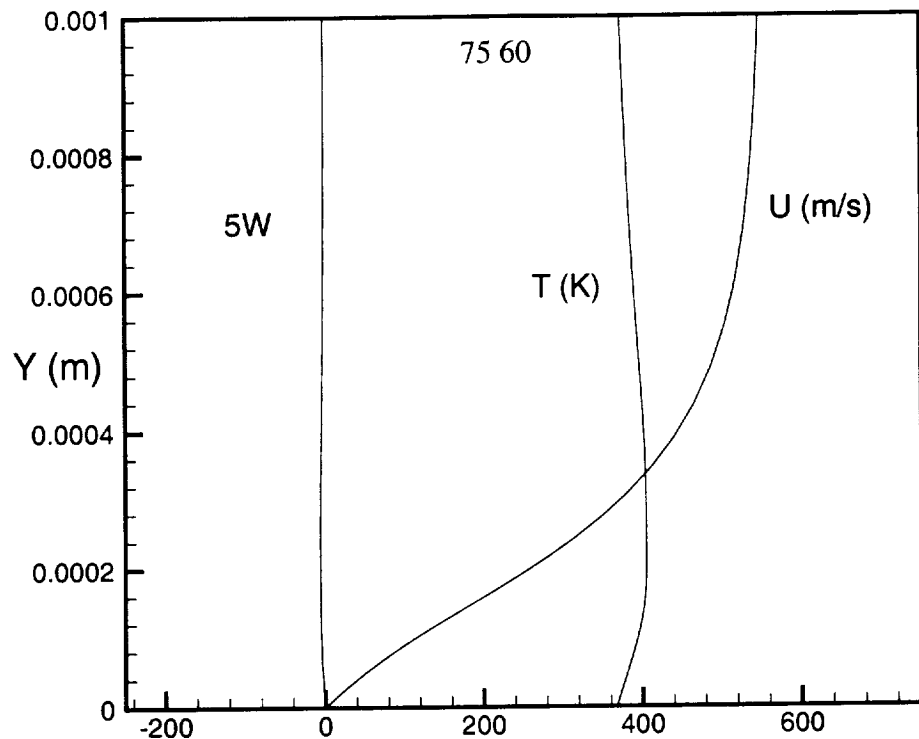


Figure 54. Boundary layer profiles $I=75$ $J=60$.

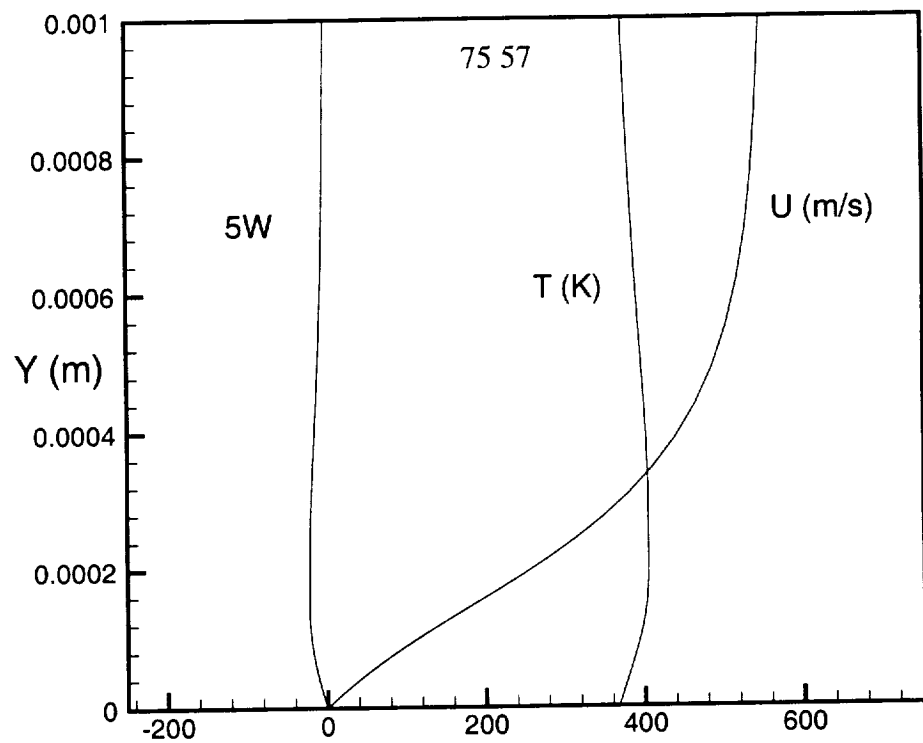


Figure 55. Boundary layer profiles $I=75$ $J=57$.

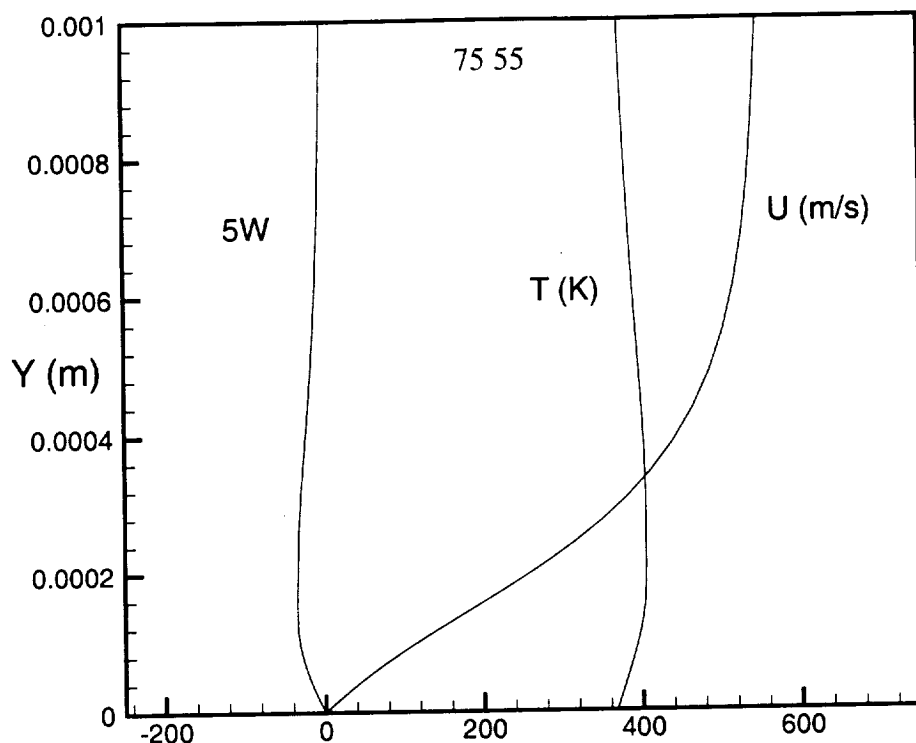


Figure 56. Boundary layer profiles $I=75$ $J=55$.

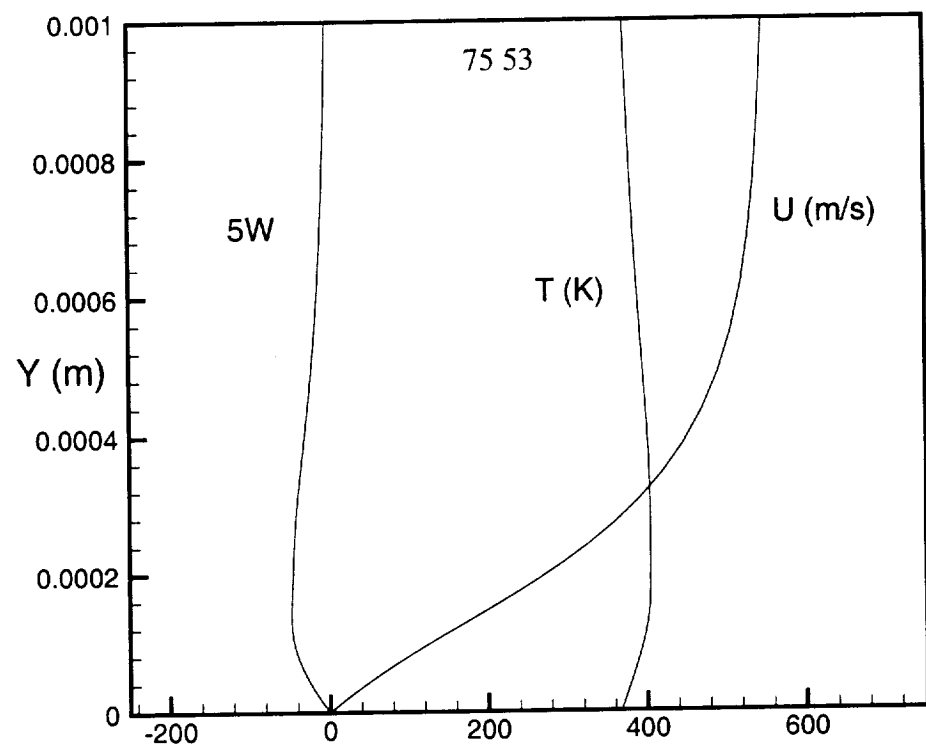


Figure 57. Boundary layer profiles $I=75$ $J=53$.

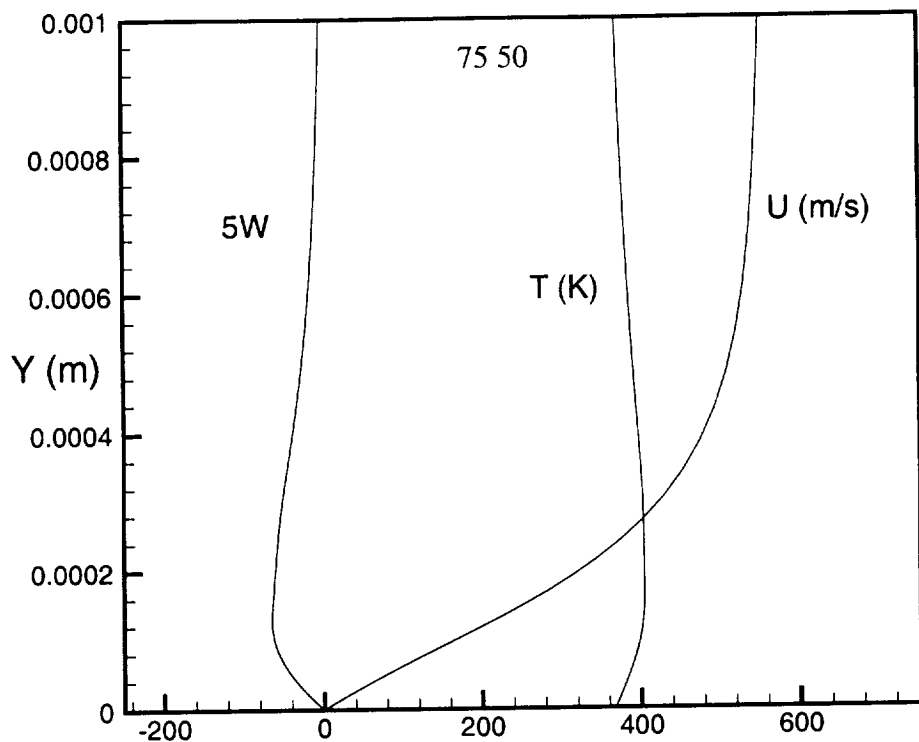


Figure 58. Boundary layer profiles $I=75$ $J=50$.

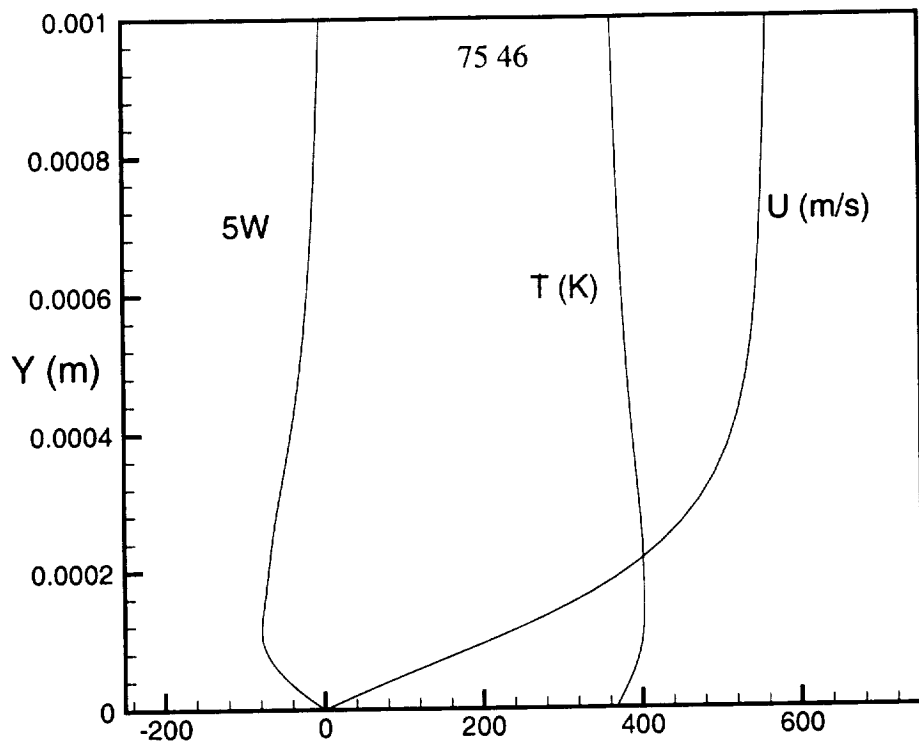


Figure 59. Boundary layer profiles $I=75$ $J=46$.

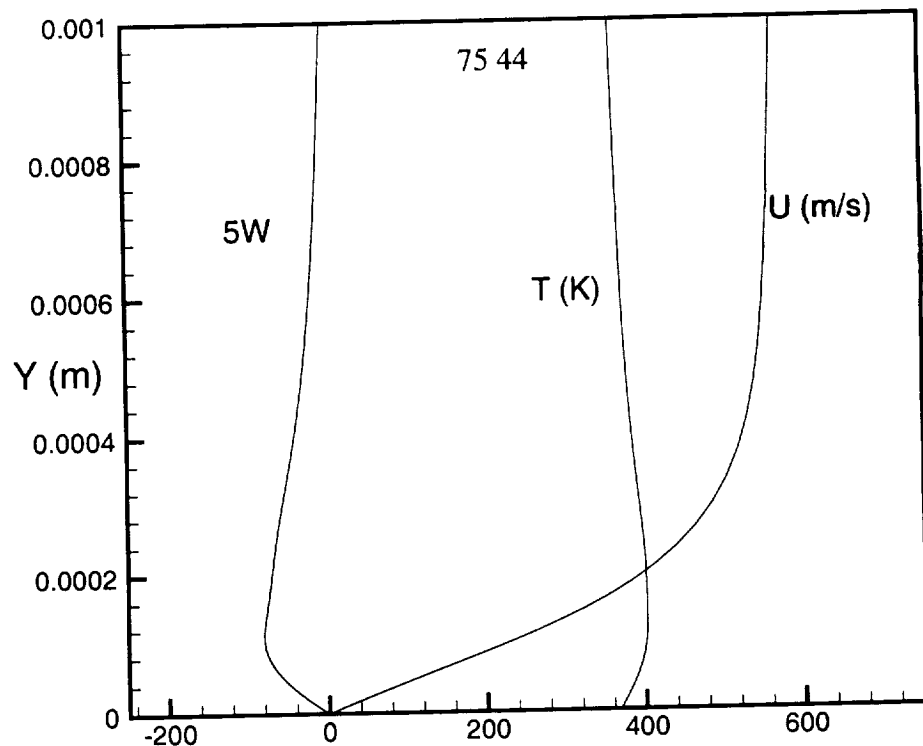


Figure 60. Boundary layer profiles $I=75$ $J=44$.

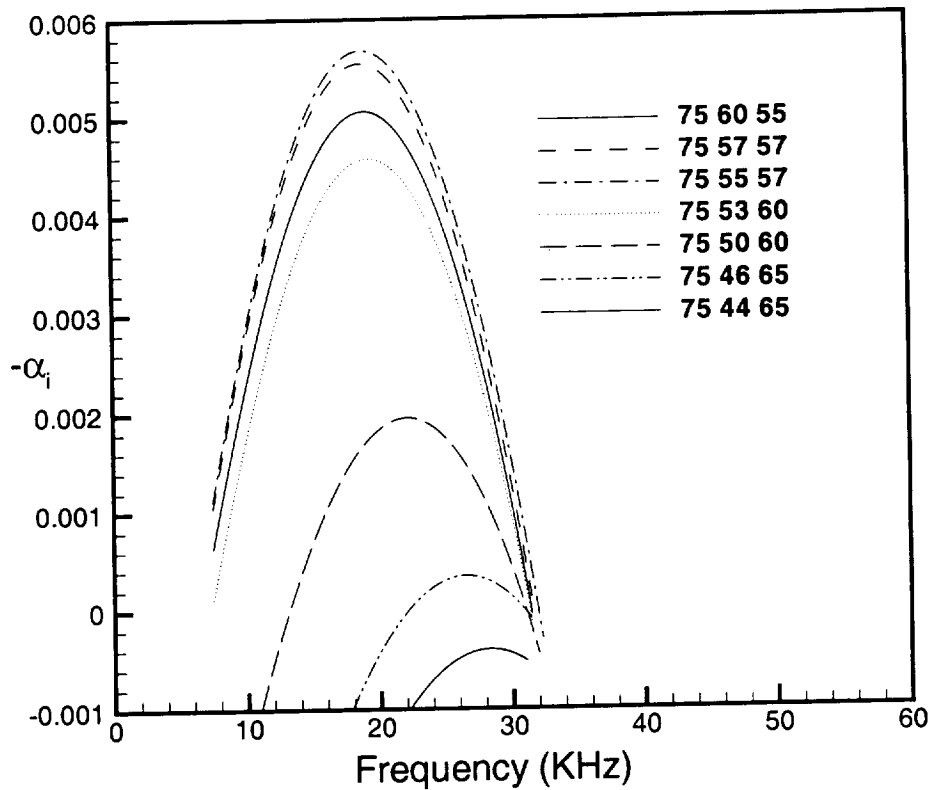


Figure 61. Growth rates from linear stability computations at $I=75$.

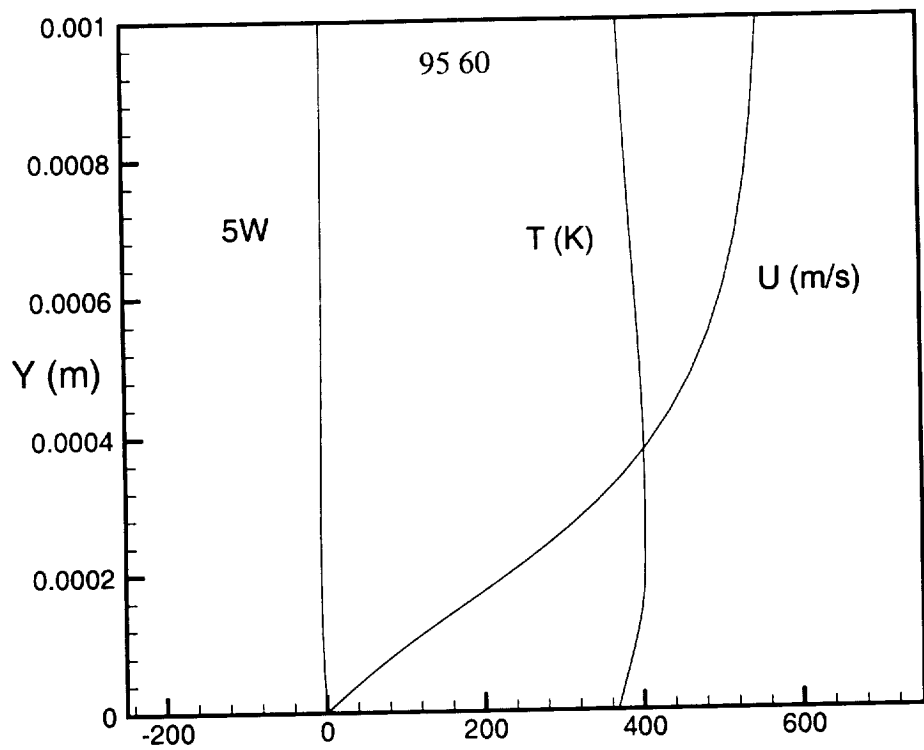


Figure 62. Boundary layer profiles $I=95$ $J=60$.

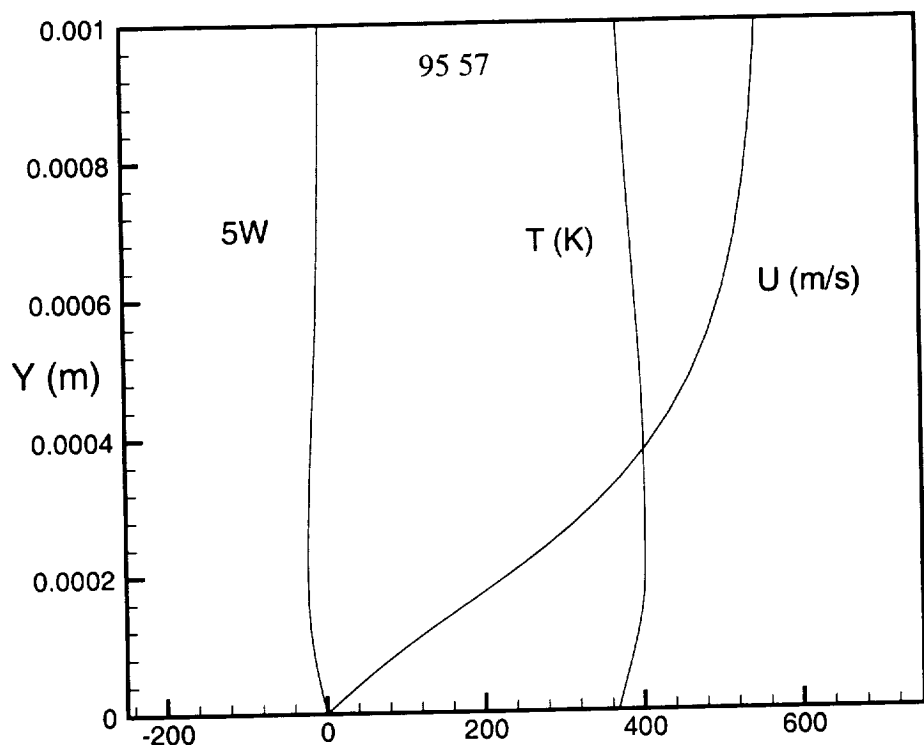


Figure 63. Boundary layer profiles $I=95$ $J=57$

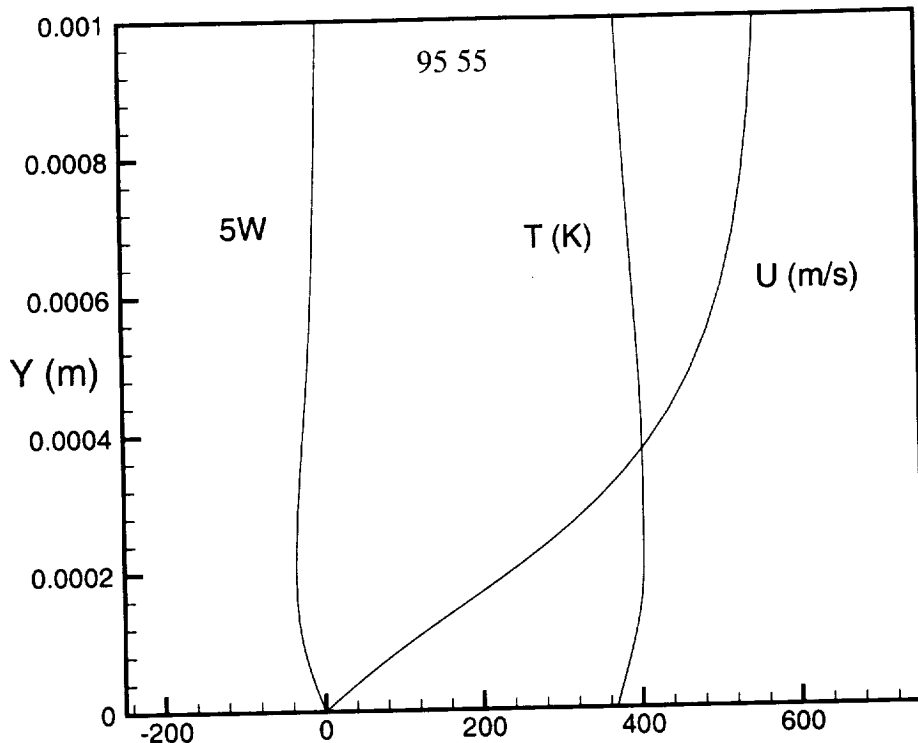


Figure 64. Boundary layer profiles $I=95$ $J=55$

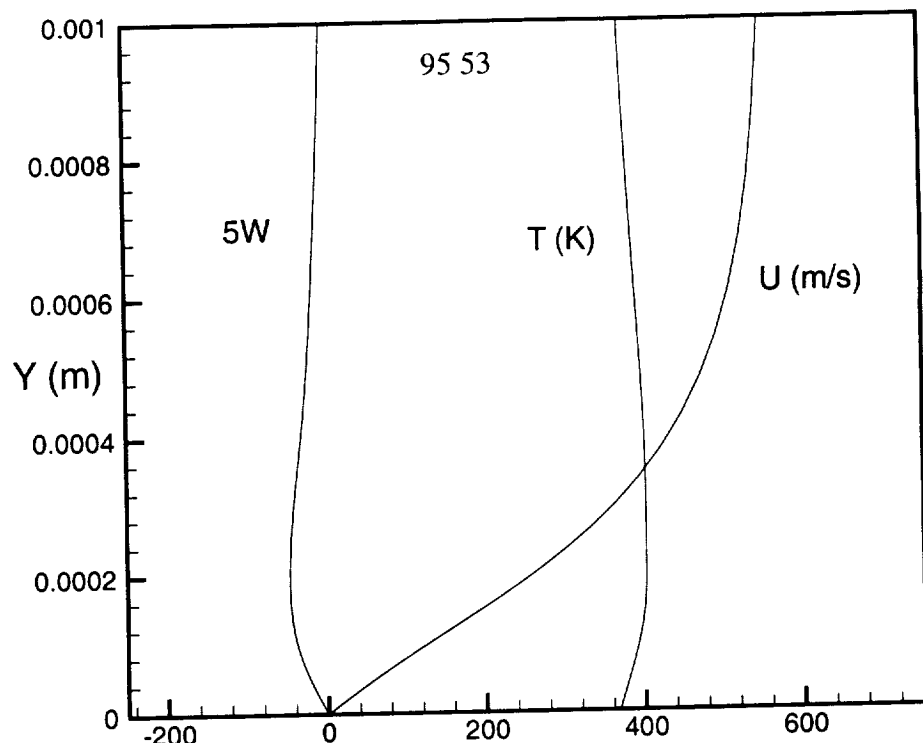


Figure 65. Boundary layer profiles $I=95$ $J=53$

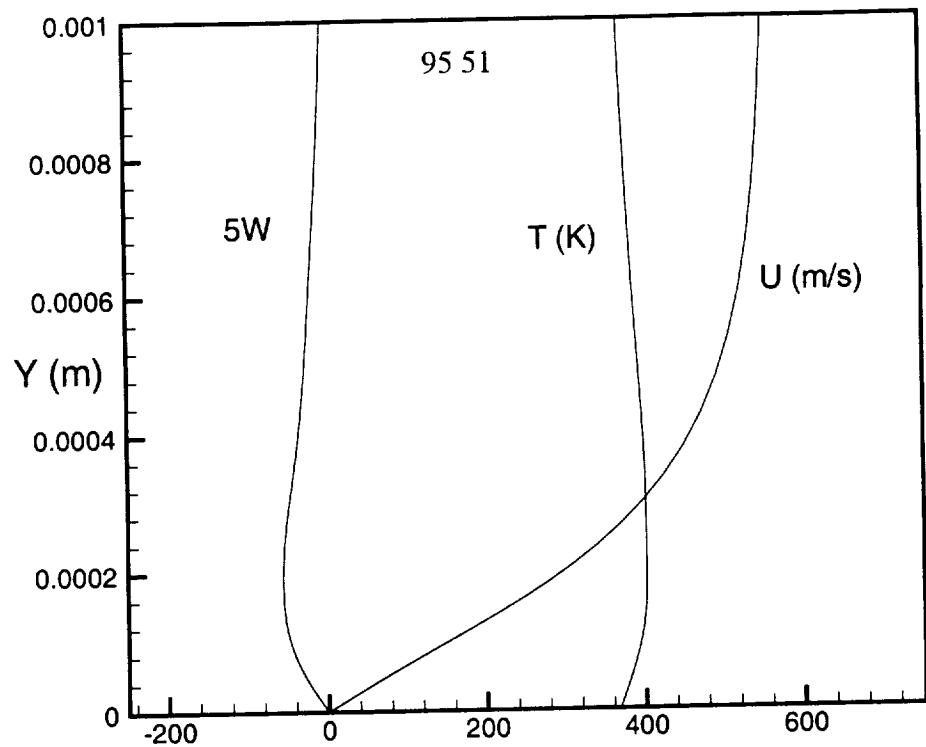


Figure 66. Boundary layer profiles $I=95$ $J=51$

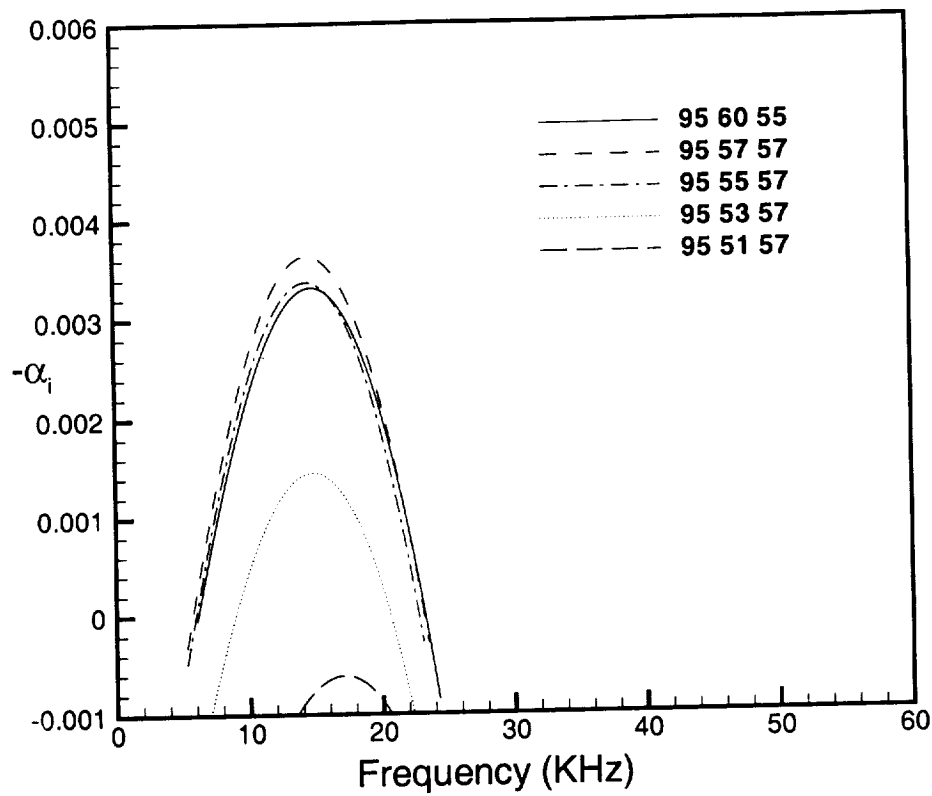


Figure 67. Growth rates from linear stability computations at $I=95$.

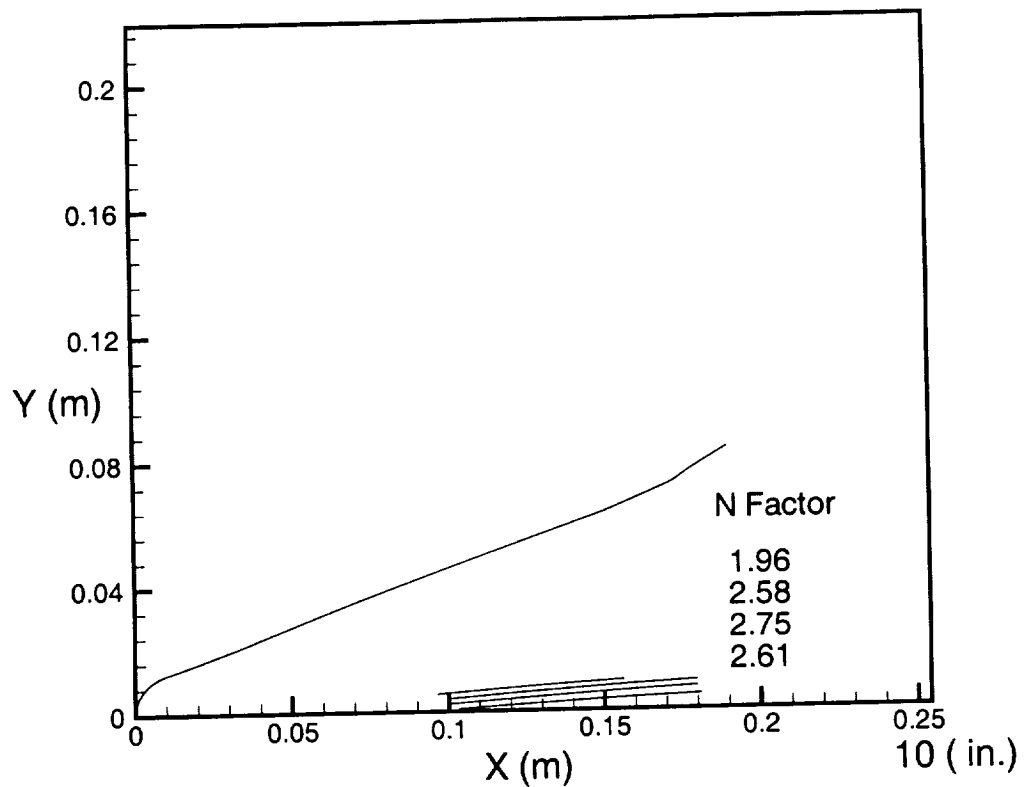


Figure 68. N - Factor traces for case 2.

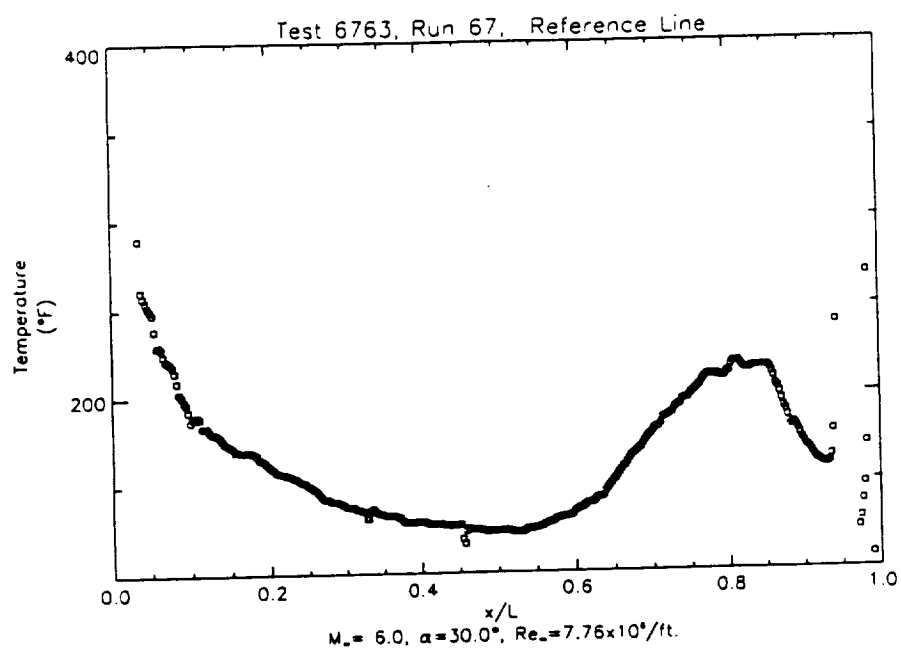


Figure 69. Experimental wall temperature measurements along the center line..

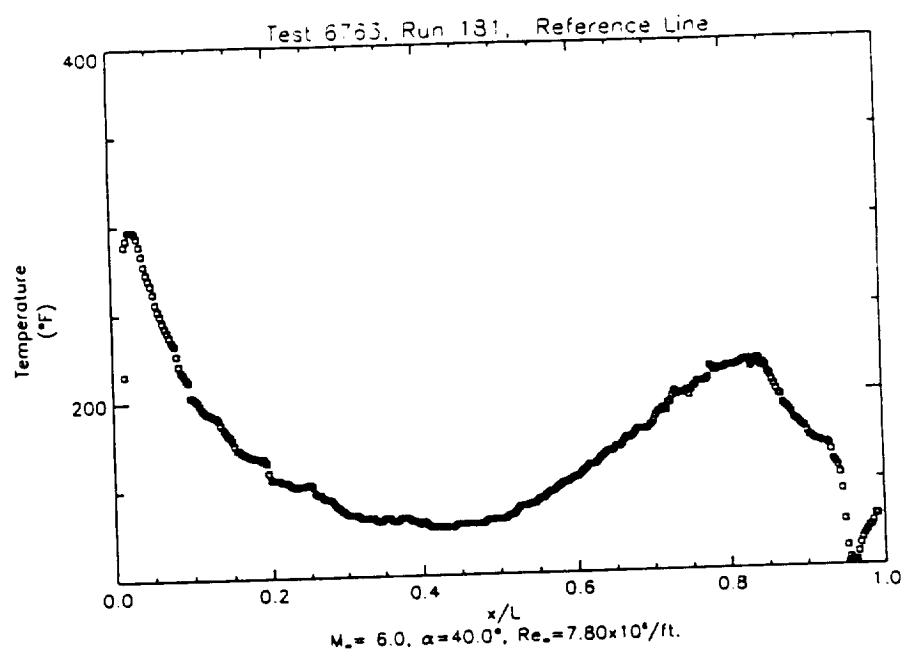
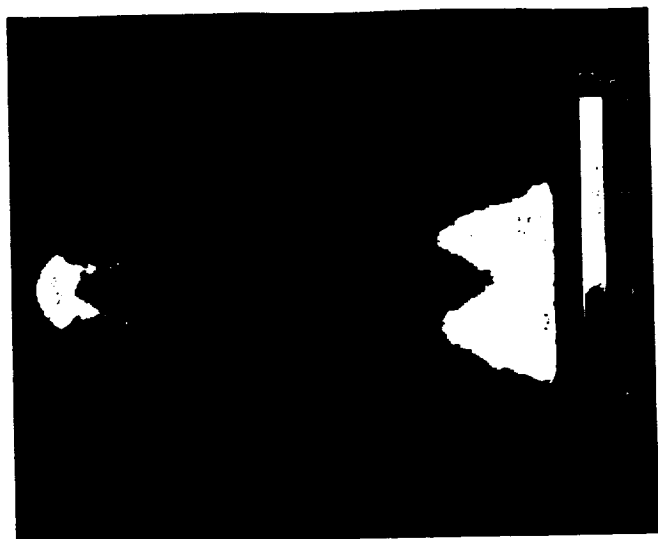
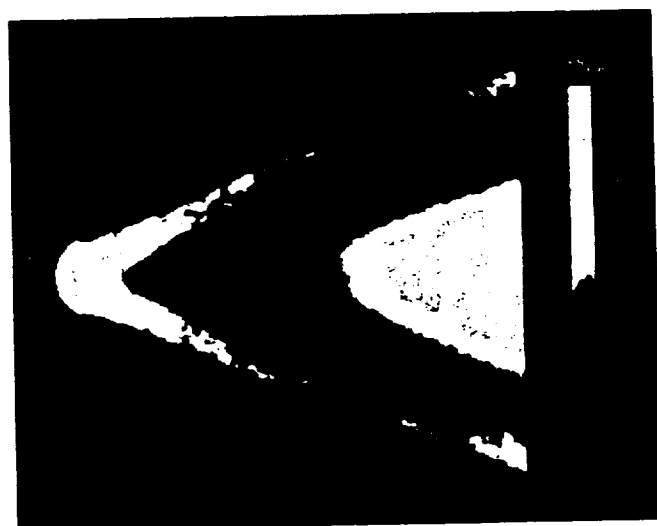


Figure 70. Experimental wall temperature measurements along the center line.



a) $\alpha=30 \deg$



b) $\alpha=40 \deg$

Figure 71. Effect of angle of attack on transition for $M=6$ and $Re=4*10^6/\text{ft}$.
(From Thompson et.al,1998)

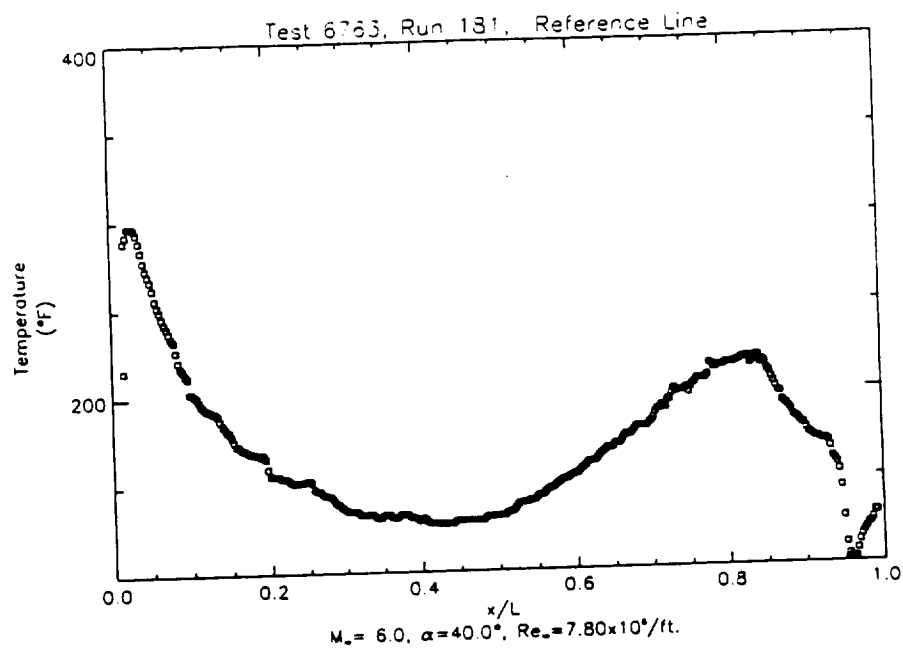
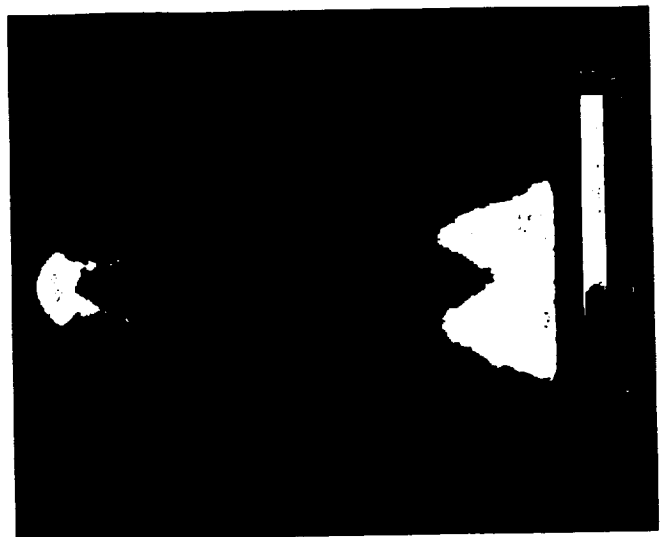


Figure 70. Experimental wall temperature measurements along the center line.



a) $\alpha=30 \text{ deg}$



b) $\alpha=40 \text{ deg}$

Figure 71. Effect of angle of attack on transition for $M=6$ and $Re=4*10^6/\text{ft.}$
(From Thompson et.al,1998)

